Inorganic Chemistry

pubs.acs.org/IC Article

Diquinol Functionality Boosts the Superoxide Dismutase Mimicry of a Zn(II) Complex with a Redox-Active Ligand while Maintaining Catalyst Stability and Enhanced Activity in Phosphate Solution

Jamonica L. Moore,[⊥] Julian Oppelt,[⊥] Laura Senft, Alicja Franke, Andreas Scheitler, Meghan W. Dukes, Haley B. Alix, Alexander C. Saunders, Sana Karbalaei, Dean D. Schwartz, Ivana Ivanović-Burmazović,* and Christian R. Goldsmith*

Cite This: *Inorg. Chem.* 2022, 61, 19983−19997 Read Online

ACCESS | Metrics & More | Article Recommendations | Supporting Information

ABSTRACT: In the current work, we demonstrate ligand design concepts that significantly improve the superoxide dismutase (SOD) activity of a zinc complex; the catalysis is enhanced when two quinol groups are present in the polydentate ligand. We investigate the mechanism through which the quinols influence the catalysis and determine the impact of entirely removing a chelating group from the original hexadentate ligand. Our results suggest that SOD mimicry with these compounds requires a ligand that coordinates Zn(II) strongly in both its oxidized and reduced forms and that the activity proceeds through Zn(II)-semiquinone complexes. The complex with two quinols displays greatly enhanced catalytic ability, with the activity improving by as much as 450% over a related complex with a single quinol. In the reduced form of the diquinol complex, one quinol appears to coordinate to the zinc much more weakly than the other. We believe that superoxide can more readily displace this portion of the ligand, facilitating its coordination to the metal center and thereby hastening the SOD reactivity. Despite the presence of two redox-active groups that may communicate through intramolecular hydrogen bonding and redox tautomerism, only one quinol undergoes two-electron oxidation to a *para*-quinone during the catalysis. After the formation of the *para*-quinone, the remaining quinol deprotonates and binds tightly to the metal, ensuring that the complex remains intact in its oxidized state, thereby maintaining its catalytic ability. The Zn(II) complex with the diquinol ligand is highly unusual for a SOD mimic in that it performs more efficiently in phosphate solution.

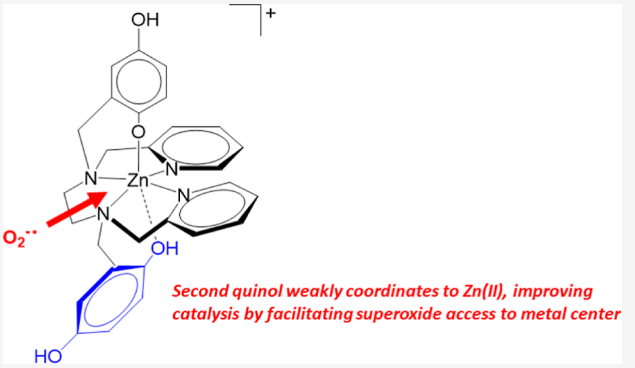

INTRODUCTION

The over-production of reactive oxygen species (ROS), such as superoxide ($O_2^{\bullet-}$) and hydrogen peroxide (H_2O_2), has been associated with a wide array of health conditions.[1−7] Although the exact contributions of ROS to these disorders remain unresolved, the development of antioxidants capable of correcting aberrant oxidative activity within the body would greatly benefit modern medicine.[8] One attractive antioxidant design strategy is to synthesize small molecules that resemble the enzymes that the body itself uses to regulate ROS concentrations. A small dose of such an antioxidant would alleviate oxidative stress by catalytically degrading one or more sorts of ROS. Investigated antioxidants include functional mimics of superoxide dismutases (SODs), which are manganese-, iron-, nickel-, or copper-containing enzymes that catalyze the degradation of $O_2^{\bullet-}$ to O_2 and H_2O_2 (eq 1).[9−17] In these enzymes, the metal cycles between two oxidation states, with the oxidized form oxidizing $O_2^{\bullet-}$ to O_2 and the reduced partner reducing $O_2^{\bullet-}$ to H_2O_2. The copper-containing SODs usually, but not always,[18] contain a Zn(II) ion in the active site. The role of the Zn(II) appears to be to stabilize the enzyme and facilitate release of the H_2O_2 product, but some catalysis is retained if the zinc is removed.[19,20]

$$2O_2^{\bullet-} + 2H^+ \rightarrow O_2 + H_2O_2 \quad (1)$$

Our laboratory has recently found that three Mn(II)-containing magnetic resonance imaging contrast agent sensors for H_2O_2 can also serve as catalysts for $O_2^{\bullet-}$ degradation.[21−25] The organic ligands of two of these probes contain quinol (hydroquinone, HQ) groups, which reversibly oxidize to *para*-quinones upon reaction with excess $O_2^{\bullet-}$ or H_2O_2 (Scheme

Received: September 13, 2022
Published: November 29, 2022

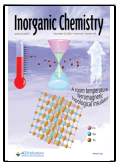

https://doi.org/10.1021/acs.inorgchem.2c03256
Inorg. Chem. 2022, 61, 19983−19997

1).[22,23,25] These catalysts differ from other SOD mimics in that the organic ligand can potentially serve as a redox partner for

Scheme 1

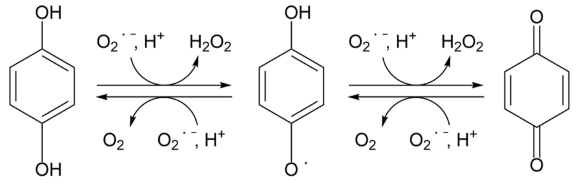

the oxidation and reduction of $O_2^{\cdot-}$; normally, the transition metal is the sole oxidant and reductant. Although metal-free *N*-(2,5-dihydroxybenzyl)-*N*,*N*′,*N*′-*tris*(2-pyridinylmethyl)-1,2-ethanediamine (H_2qp1, Scheme 2) cannot catalyze superoxide degradation by itself, $[Zn(H_2qp1)(OTf)]^+$ (**1**) is a viable catalyst, with activity comparable to those of manganese-containing SOD mimics.[26] The activity is further notable because it is amplified in phosphate buffer; phosphate anions competitively inhibit most manganese-containing SOD mimics.[24,27,28] Because Zn(II) cannot readily change oxidation states, the H_2qp1 ligand was proposed to be the relevant redox partner for $O_2^{\cdot-}$ and cycle through three different forms, containing either a quinol (HQ), a quinoxyl radical (semiquinone, SQ), or a *para*-quinone (Scheme 1). The catalytic activity of this compound demonstrates that the dual roles of the transition metal ion in traditional SOD mimicry—electrostatically attracting $O_2^{\cdot-}$ and transferring electrons to or from the substrate—can instead be fulfilled by a complex consisting of a redox-inactive metal ion and a redox-active ligand.

There are many benefits to such an approach. First, it allows innocuous metal ions to be used in the place of more toxic redox-active transition metals, such as iron and manganese. Second, Zn(II) complexes tend to be more stable than their Mn(II) and Fe(II) analogues,[29,30] which should prolong catalysis. Due to these first two factors, the study of manganese-containing SOD mimics has been heavily centered around complexes with macrocyclic ligands, which can be difficult to synthesize and modify. Even with these measures, these compounds tend to have limited stability in aqueous solutions.[31−33] A third, and unanticipated, benefit is the aforementioned enhanced activity of **1** in phosphate solution. This is a significant advantage because mammalian cells contain high levels of phosphate.[34,35]

The development of additional complexes is essential to determine how the molecular structure can impact function, for even subtle changes to the ligand may substantially alter the activity. The H_2qp1 ligand is hexadentate and is capable of fully coordinating the Zn(II) by itself.[26] Previously obtained mass spectrometry data suggest that **1** reacts with $O_2^{\cdot-}$ through an inner-sphere mechanism. Replacing H_2qp1 with a pentadentate ligand or replacing one of the nitrogen atoms with a weaker oxygen atom donor could potentially improve the activity by introducing a more accessible site for superoxide coordination. The structural and potentiometric pH titration data that we have previously obtained for Mn(II) and Zn(II) complexes suggest that quinols are poor ligands but that deprotonation to the quinolate form markedly improves their metal-binding affinity.[22,26] The installation of a second redox-active quinol into the ligand may improve the activity either by better ensuring that a quinol remains bound to the Zn(II) at all times or by providing a donor atom that is easier to displace if one of the quinols remains protonated. Furthermore, the additional quinol may serve to protect the catalyst from inadvertent oxidation and deactivation by ROS by providing a sacrificial reductant; **1** was found to degrade when the concentration of H_2O_2 became too high.[26] In order to develop structure−function relationships for this new class of SOD mimic, we have therefore prepared Zn(II) complexes with *N*,*N*′-(2,5-dihydroxybenzyl)-*N*,*N*′-*bis*(2-pyridinylmethyl)-1,2-ethanediamine (H_4qp2) and *N*-(2,5-dihydroxybenzyl)-*N*,*N*′-*bis*(2-pyridinylmethyl)-1,2-ethanediamine (H_2qp3, Scheme 2). The former ligand was previously used in a redox-responsive MRI contrast agent, whereas the potentially pentadentate H_2qp3 was the immediate precursor in its synthesis.[22]

The complex with two quinols, $[Zn(H_4qp2)]^{2+}$ (**2**), is more active than **1** and likewise performs better as a catalyst in phosphate buffer, whereas $[Zn(H_2qp3)(H_2O)]^{2+}$ (**3**) does not noticeably hasten $O_2^{\cdot-}$ degradation beyond the uncatalyzed reaction. Simply mixing zinc salts and quinols together is therefore not sufficient to achieve SOD mimicry. The relative activities of the three Zn(II)-quinol complexes can be rationalized by the speciation of the complexes in water and the observed end-products of oxidation by $O_2^{\cdot-}$. Complex **2** also differs from **1** in that it can react with O_2; this represents a rare instance of a redox-inactive metal activating dioxygen.[36]

EXPERIMENTAL SECTION

Materials. All chemicals and solvents were purchased from Sigma-Aldrich and used as received unless otherwise noted. 2,2-Diphenyl-1-picryl-hydrazyl hydrate (DPPH) was supplied by EMD Millipore. All deuterated solvents were bought from Cambridge Isotopes. Diethyl ether (ether) and methanol (MeOH) were bought from Fisher. Methylene chloride (CH_2Cl_2) was purchased from Mallinckrodt Baker. *N*,*N*′-*Bis*(2,5-dihydroxybenzyl)-*N*,*N*′-*bis*(2-pyridinylmethyl)-1,2-ethanediamine (H_4qp2) and *N*-(2,5-dihydroxybenzyl)-*N*,*N*′-*bis*(2-pyridinylmethyl)-1,2-ethanediamine (H_2qp3) were previously prepared.[22]

Instrumentation. All ^{1}H and ^{13}C NMR spectra were recorded on a 400 MHz or 600 mHz AV Bruker NMR spectrometer. In each spectrum, the reported NMR resonance peak frequencies were

Scheme 2

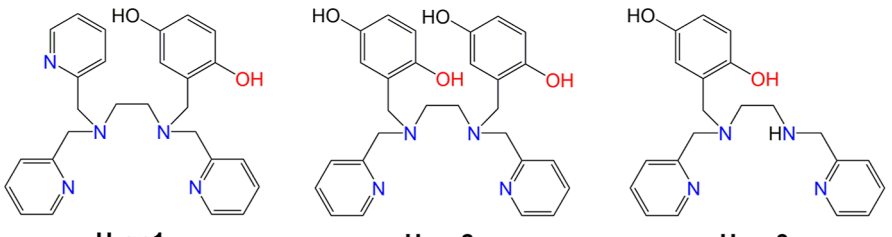

https://doi.org/10.1021/acs.inorgchem.2c03256
Inorg. Chem. 2022, 61, 19983−19997

referenced to internal standards, such as solvent resonances. A Bruker EMX-6/1 X-band electron paramagnetic resonance (EPR) spectrometer operated in the perpendicular mode was used to collect EPR data, which were subsequently analyzed with the program EasySpin. All EPR samples were run as frozen solutions in quartz tubes. Optical data were collected on a Varian Cary 50 spectrophotometer and analyzed using software from the WinUV Analysis Suite. High-resolution mass spectrometry data were obtained at the Mass Spectrometer Center at Auburn University on a Bruker microflex LT MALDI-TOF mass spectrometer via direct probe analysis operated in the positive ion mode. Infrared spectroscopy (IR) data were obtained with a Shimadzu IR Prestige-21 FT-IR spectrophotometer. Cyclic voltammetry (CV) was performed under N_2 at 294 K using an Epsilon electrochemistry workstation (Bioanalytical System, Inc.), a gold working electrode, a platinum wire auxiliary electrode, and a silver/silver (I) chloride reference electrode. All elemental analyses (C, H, and N) were performed by Atlantic Microlabs (Norcross, GA); crystalline samples were dried under vacuum and placed under a N_2 atmosphere prior to shipment.

X-ray Crystallography. Structural data on single crystals were collected using a Bruker D8 VENTURE κ-geometry diffractometer system equipped with an Incoatec IμS 3.0 microfocus sealed tube (Mo Kα, λ = 0.71073 Å) and a multilayer mirror monochromator. SMART (v 5.624) was used to determine the preliminary cell constants and control data acquisition. The Bruker SAINT software package was used to determine integrated intensities; the data were corrected for absorption effects using the multi-scan method (SADABS). The structure was solved and refined using the Bruker SHELXTL software package. All non-hydrogen atoms were refined anisotropically. Hydrogen atoms were included at idealized positions 0.95 Å from their parent atoms prior to the final refinement. Further details regarding the data acquisition and analysis are included in the Supporting Information as well as Table 1.

Table 1. Selected Crystallographic Data for 2 and 3[a]

parameter	$[Zn(H_4qp2)](OTf)_2$ (2)	$[Zn(H_2qp3)(H_2O)](OTf)_2$ (3)
formula	$C_{30}H_{30}F_6N_4O_{10}S_2Zn$	$C_{23}H_{27}F_6N_4O_{10}S_2Zn$
MW	850.07	762.97
crystal system	triclinic	monoclinic
space group	$P\bar{1}$	$P121/n1$
a (Å)	11.5601(4)	11.5256(4)
b (Å)	11.9171(4)	12.4789(4)
c (Å)	13.8096(5)	21.6728(7)
α (°)	100.936(2)	90
β (°)	105.707(2)	90.4010(10)
γ (°)	105.978(2)	90
V (Å^3)	1687.37(10)	317.05(18)
Z	2	4
crystal color	colorless	colorless
T (K)	100(2)	110(2)
reflns collected	57,040	93,868
unique reflns	16,337	16,779
$R1$ (F, $I > 2\sigma(I)$)	0.0517	0.0454
$wR2$ (F^2, all data)	0.1375	0.1256

[a] $R1 = \Sigma||F_o| - |F_c||/\Sigma|F_o|$; $wR2 = [\Sigma w(F_o^2 - F_c^2)^2/\Sigma w(F_o^2)^2]^{1/2}$.

Potentiometric Titrations. The speciation chemistry of the Zn(II) complexes in water was assessed using a METROHM 765 Dosimat with a jacketed, airtight glass titration vessel. A Fisher Scientific Accumet Research AR15 pH meter was used to determine the pH of the sample solutions during the titrations. The electrode was calibrated before each titration using commercially available standard solutions buffered to pH 4.0, 7.0, and 10.0. All samples were purged with argon prior to analysis and subsequently analyzed under an argon atmosphere at 25 °C. All solution samples were prepared in solutions of 100 mM KCl in deionized Millipore water. The titrations investigating metal−ligand speciation were run with solutions that contained a 1:1 molar mixture of the ligand and $Zn(OTf)_2$. Carbonate-free solutions of 0.10 M KOH and 0.10 M HCl were prepared using argon-saturated deionized Millipore water. Initially, we estimated pK_a values through visual inspection of the data plotted in KaleidaGraph v. 4.0. We subsequently attempted to analyze and fit the data to speciation models using the Hyperquad2006 program.[37]

Analysis of the Antioxidant Properties of the Coordination Complexes. We previously screened the abilities of other coordination complexes to catalytically degrade superoxide using the xanthine oxidase/hypoxanthine/lucigenin assay.[22,23,38] The superoxide was generated in situ from a reaction between xanthine and xanthine oxidase. A subsequent reaction between O_2^- and lucigenin provides a spectroscopic signal that can be used to quantify an antioxidant's ability to degrade O_2^-. The copper/zinc superoxide dismutase isolated from bovine erythrocytes (0.001−100 U/mL, Calbiochem) served as a positive control. Each assay was carried out in a total volume of 1 mL containing 50 mM Tris (pH 8.0), hypoxanthine (50 μM), xanthine oxidase (0.005 U/mL, Calbiochem), and dark-adapted lucigenin (5 μM) in the presence of either the studied Zn(II) complex (0.1 nM−10 μM) or its vehicle. Reactions were carried out at room temperature and were initiated by the addition of xanthine oxidase to the hypoxanthine-containing solution. Luminescence was measured using a TD-20/20 (Turner Designs) luminometer and expressed as relative light units (RLUs). Luminescence was measured for four 10 s integrations after an initial delay of 3 s. The four RLU values were averaged, and each concentration was expressed as a percent of that produced in the presence of vehicle. Duplicates of each data point were collected, and the entire assay was performed three times.

We also assessed the antioxidant activities of the Zn(II) complexes through the DPPH assay (DPPH = 2,2-diphenyl-1-picrylhydrazyl radical hydrate).[39−41] In this assay, potential antioxidants are tested for their abilities to donate hydrogen atoms to the radical to generate the corresponding hydrazine. Aqueous solutions of either **2**, **3**, or ascorbic acid were added to a solution of 0.10 mM DPPH in MeOH, such that the final reaction volume was 0.2 mL. Samples were incubated in the dark for 30 min at room temperature before being spectrophotometrically analyzed on a Molecular Devices Spectramax Plus. The absorbance at 517 nm, the λ_{max} of the hydrazine product, was recorded. Experiments were performed in triplicate.

Determination of In Vitro SOD Activity via Stopped-Flow Kinetics. The abilities of the Zn(II) complexes to catalytically degrade superoxide were more thoroughly tested by a direct method using stopped-flow techniques that have been more fully described in prior work from one of our laboratories.[27] Stopped-flow measurements were performed on a Biologic SFM-400 four syringe stopped-flow system using only the first three syringes and a Berger Ball mixer to minimize mixing effects between aqueous buffered solutions and DMSO solutions of KO_2. A J&M TIDAS S MMS UV/VIS diode array detector (integration time 0.5 ms, 180−720 nm wavelength) and an Energetiq LDLS ENQ EQ-99-FC laser-driven light source were used.

Superoxide solutions were prepared by suspending 220−240 mg KO_2 in 20 mL of dry DMSO. The suspension was stirred for at least 30 min under an inert atmosphere before the suspension was filtered through a PTFE syringe filter (Ø = 0.45 μm) to give a saturated KO_2 solution, which was transferred to the stopped flow setup. The potential SOD mimics (SODm) were dissolved in aqueous solutions buffered to either pH 7.4 or 8.1. The buffers were prepared from Millipore water and either 4-morpholinepropanesulfonic acid (MOPS) or sodium dihydrogen phosphate. The concentration of the buffer was 60 mM, and the ionic strength was adjusted to 150 mM for each solution through the addition of NaCl. All of the buffered solutions were treated with Chelex 100 sodium exchange resin for at least 24 h before use in order to remove adventitious metal ions. Stock solutions containing 0.10 mM of each tested SODm were prepared in each buffer; if necessary, the stock solution contained 10% DMSO to ensure that the complexes dissolved fully. The stock solutions were

https://doi.org/10.1021/acs.inorgchem.2c03256
Inorg. Chem. 2022, 61, 19983−19997

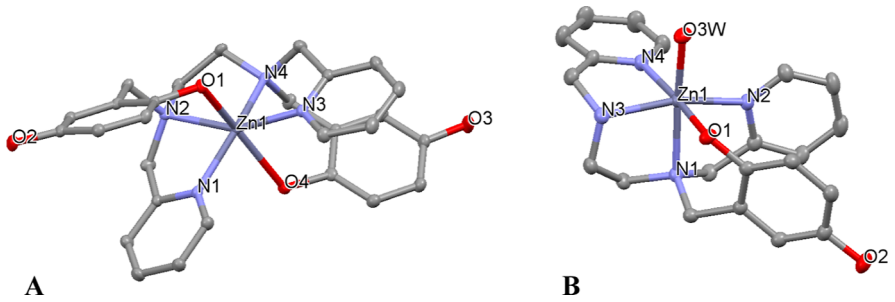

Figure 1. Thermal ellipsoid plots of (A) $[Zn(H_4qp2)]^{2+}$ and (B) $[Zn(H_2qp3)(H_2O)]^{2+}$. Ellipsoids set at 50% probability. All hydrogen atoms, triflate counteranions, and non-bound solvent molecules have been omitted for clarity.

diluted in buffer to give a series of SODm concentrations suitable for the stopped-flow experiments.

Kinetic measurements were performed adding a large excess of superoxide to the putative SOD mimetic: $[O_2^{\cdot-}]$ = 100−200 μM, [SODm] = 0.25−4.5 μM. The aqueous solution containing the studied Zn(II) complex was mixed in a 9:1 ratio with the superoxide solution in DMSO using a high-density mixer. In each experiment, the concentration of superoxide exceeded that of the zinc-containing catalyst by at least 10-fold to ensure catalytic conditions. The starting concentrations of superoxide were determined before each measurement from the absorbance at 250 nm—the characteristic λ_{max} for the superoxide band—and the documented molar extinction coefficient for $O_2^{\cdot-}$ at this wavelength (ε = 2257 M^{-1} cm^{-1} at pH 7.4 and 7.8 or ε = 2260 M^{-1} cm^{-1} for pH 8.1).[42] All kinetic data were fit with the program Biokine 32 V4.80. Each k_{obs} value represents an average of at least nine measurements. Each k_{cat} was determined from the slope of k_{obs} versus [SODm]. All measurements were performed at 21 °C.

Cryospray-Ionization Mass Spectrometry. Cryospray-ionization mass spectrometry (CSI-MS) measurements were performed on a UHR-TOF Bruker Daltonik maXis Plus, an ESI-quadrupole time-of-flight (qToF) mass spectrometer capable of a resolution of at least 60.000 (FWHM), which was coupled to a Bruker Daltonik Cryospray unit. The detector was run in the positive ion mode with a source voltage of 3.5 kV and a flow rate of 240 μL/h. The temperatures of the N_2 spray gas and the dry gas used for solvent removal were −40 and −35 °C for superoxide experiments and 0 and 0 °C for hydrogen peroxide experiments, respectively. The mass spectrometer was calibrated prior to each experiment via direct infusion of an Agilent ESI-TOF low concentration tuning mixture, which provided a m/z range of singly charged peaks up to 2700 Da in both ion modes. For the reactions with $O_2^{\cdot-}$, 1 × 10^{-5} M solutions of each compound in MeCN were cooled to −40 °C and mixed with excess solid KO_2. For the reactions with H_2O_2, 1 × 10^{-5} M solutions of each coordination complex in MeCN were cooled to 0 °C and mixed with the given amount of H_2O_2. Aliquots from the resultant mixtures were then injected into the mass spectrometer. To ensure the survival of metastable reaction species generated at low temperatures, the injection syringe and the tubing of the mass spectrometer were precooled with tempered solvent (0 °C or −40 °C, respectively). After tempering, the reaction solutions were injected as quickly as possible, with the recording of mass spectrometry data commencing immediately afterward. Multiple samples were collected and analyzed over time to determine whether the product distribution was changing during the course of the reaction. Aliquots were also analyzed after the reactions warmed to room temperature. The solvents were not rigorously dried in order to ensure a source of protons. The measured data were processed and analyzed with Bruker Data Analysis 5.2.

Syntheses. *[N,N′-Bis(2,5-Dihydroxybenzyl)-N,N′-bis(2-pyridinylmethyl)-1,2-ethanediamine]zinc (II) Triflate {[Zn(H_4qp2)](OTf)$_2$, 2}.* The H_4qp2 ligand (213 mg, 0.434 mmol) and $Zn(OTf)_2$ (159 mg, 0.434 mmol) were dissolved in 3 mL of acetonitrile (MeCN) under N_2. The solution was stirred for 16 h at 60 °C. After the solution was cooled to room temperature (RT), ether was gradually added to precipitate the product as a white powder (264 mg, 71%). CH_2Cl_2 was gradually added to a saturated solution of the product in MeOH to yield crystals suitable for single-crystal X-ray diffraction. ^{1}H NMR (400 MHz, CD_3CN, 293 K): δ 8.73 (d, J = 5.4 Hz, 2H), 7.92−8.03 (m, 3H), 7.54 (t, J = 6.4 Hz, 2 H), 7.32−7.45 (m, 5H), 4.39 (d, J = 16.4 Hz, 2H), 4.09−4.27 (m, 1H), 3.72−3.91 (m, 6H), 3.43 (d, J = 13.6 Hz, 2H), 3.22 (s, 1H), 2.75 (d, J = 10.9 Hz, 2H), 2.60 (d, J = 11.1 Hz, 2H). ^{13}C NMR (100 MHz, CD_3CN, 293 K): δ 155.11, 150.56, 147.86, 147.83, 141.11, 132.30, 131.29, 128.73, 125.01, 124.94, 57.38, 52.87. Optical spectroscopy (MeCN, 293 K): 298 nm (ε = 2400 M^{-1} cm^{-1}), 262 nm (ε = 2500 M^{-1} cm^{-1}). IR (KBr, cm^{-1}): 3406 (m), 3144 (m), 1653 (w), 1612 (m), 1576 (w), 1508 (w), 1458 (w), 1400 (s), 1385 (s), 1252 (m), 1157 (m), 1101 (w), 1032 (s), 943 (w), 920 (w), 878 (w), 824 (m), 766 (s), 638 (s), 577 (m), 517 (s), 419 (m). MS (ESI): Calcd for $[Zn(H_3qp2)]^+$, 549.1481, $[Zn(H_4qp2)(OTf)]^+$, 699.1079; Found, 549.1415, 699.1237. Elemental analysis: Calcd for $C_{30}H_{30}N_4F_6O_{10}S_2Zn{\cdot}H_2O$: C, 41.51%; H, 3.72%; N, 6.45%. Found: 41.30%; H, 3.37%; N, 6.32%.

Aqua[N-(2,5-Dihydroxybenzyl)-N,N′-bis(2-pyridinylmethyl)-1,2-ethanediamine]zinc (II) Triflate {[Zn(H_2qp3)(H_2O)](OTf)$_2$, 3}. The H_2qp3 ligand (166 mg, 0.456 mmol) and $Zn(OTf)_2$ (166 mg, 0.456 mmol) were dissolved in 3 mL of MeCN under N_2. The solution was stirred for 16 h at 60 °C. Ether was added to the solution as it cooled to RT to deposit the product as a white crystalline powder (267 mg, 78% yield). Gradually adding ether to a saturated MeCN solution resulted in crystals that were suitable for single-crystal X-ray diffraction. ^{1}H NMR (400 MHz, CD_3CN, 293 K): δ 8.84 (d, J = 4.8 Hz, 1H) 8.56 (d, J = 4.4 Hz, 1H), 8.39−7.98 (m, 4 H), 7.64−7.35 (m, 6H), 4.54−4.48 (m, 2H), 4.28 (d, J = 16.4 Hz, 2H), 3.73 (t, J = 13.2 Hz, 2H), 3.54 (d, J = 13.3 Hz, 2H), 3.08−3.04 (m, 2H), 2.95 (d, J = 13.2 Hz, 1H). ^{13}C NMR (100 MHz, CD_3CN, 293 K): δ 154.86, 151.18, 147.31, 140.66, 124.42, 121.22, 79.42, 52.97. Optical spectroscopy (MeCN): 295.9 nm (ε = 908 M^{-1} cm^{-1}), 262 nm (ε = 2094 M^{-1} cm^{-1}). IR (KBr, cm^{-1}): 3507 (w), 3134 (m), 1686 (w), 1611 (w), 1508 (w), 1400 (s), 1385 (s), 1260 (m), 1179 (m), 1096 (w), 1032 (s) 876 (w), 860 (w), 820 (w) 800 (w), 766 (m), 727 (w), 646 (s), 581 (m), 521 (s), 415 (m). MS (ESI): Calcd for $[Zn(Hqp3)]^+$, 427.1113, $[Zn(H_2qp3)(OTf)]^+$, 577.0711; found, 427.1127, 577.0742. Elemental analysis (crystals): Calcd for $C_{23}H_{24}N_4F_6O_8S_2Zn{\cdot}2H_2O$: C, 36.16%; H, 3.69%; N, 7.33%. Found: C, 36.12%; H, 3.74%; N, 7.11%.

RESULTS

Synthesis. In a prior publication from our laboratory, we reported the synthesis of both the H_4qp2 and H_2qp3 ligands and the chemistry of a Mn(II) complex with H_4qp2.[22] The triflic acid salt of the H_2qp3 ligand, which was the immediate precursor to H_4qp2, was structurally characterized in that report.

Zn(II) complexes with the H_2qp2 and H_2qp3 ligands can be prepared by dissolving a 1:1 mixture of the ligand and $Zn(OTf)_2$ in hot MeCN. Adding diethyl ether to these solutions precipitates $[Zn(H_4qp2)](OTf)_2$ (**2**) and $[Zn(H_2qp3)(H_2O)](OTf)_2$ (**3**) in high yields (>70%) and purities. The compositions were established by both

https://doi.org/10.1021/acs.inorgchem.2c03256
Inorg. Chem. 2022, 61, 19983−19997

crystallography and elemental analysis. The only challenging aspect about the syntheses is that $Zn(OTf)_2$ is poorly soluble in MeCN, necessitating both the elevated temperature (60 °C) and the lengthy reaction time (16 h). The 1:1 stoichiometry must be strictly observed because any excess $Zn(OTf)_2$ will also precipitate under the isolation conditions and contaminate the desired products. As anticipated, the products are diamagnetic and colorless. The ^{1}H NMR spectra of crystalline samples of both Zn(II) complexes in CD_3CN (Figures S1 and S5) contain more features than anticipated from the crystal structures, and each complex appears to exist as a mixture of conformers and/or coordination isomers in solution. Similarly complicated speciation in solution was also noted for $[Zn(H_2qp1)(OTf)](OTf)$ (**1**).[26]

Structural Characterization. The complexes can be crystallized from either $MeOH/CH_2Cl_2$ or MeCN/ether solutions (Figure 1). The structures differ substantially from the two Zn(II) complexes crystallized from **1**, $[Zn(H_2qp1)(MeCN)](OTf)_2$ and $[Zn(H_2qp1)(OTf)](OTf)$, in that the quinols are bound directly to the metal center.[26] Both of the new structures feature a 2:1 ratio of triflates to Zn(II)-ligand subunits, suggesting that all of the quinols remain protonated. The C−O bonds range from 1.36 to 1.39 Å, confirming both that the quinols have not been inadvertently oxidized and that each of the O−H groups remains protonated.[22,23,43]

In the structure of **2**, the H_4qp2 ligand binds in a hexadentate fashion, accounting for all six of the donor atoms in the coordination sphere of the metal ion. Overall, the Zn(II) is chelated in a highly distorted octahedral geometry, with the two quinols *trans* to each other and the two pyridines approximately *cis* to each other. There are two significant distortions from octahedral geometry. First, the bond angle between the two pyridine N-donors, N(1)-Zn(1)-N(3), is 122°; the larger space between the pyridines makes the structure somewhat resemble a pentagonal bipyramid with a missing equatorial vertex. The quinols shift slightly from their ideal octahedral positions toward the gap between the pyridine rings, resulting in a 163° O−Zn(II)−O bond angle. Second, one of the quinols is bound much more weakly than the other, with Zn−O(1) and Zn−O(4) having bond lengths of 2.196 and 2.364 Å, respectively. Each quinol appears to be hydrogen bonded to two triflates. The extensive hydrogen bonding network results in a relatively dense crystal (1.673 g/cm^3). Each quinol is approximately parallel to a pyridine ring, which may suggest aromatic interactions between these groups. The centroids of the aromatic rings are 3.73 and 3.89 Å apart, with the pyridine-containing N(3) and the quinol-containing O(4) being slightly closer together.

The structure of **3** likewise features the quinol-containing ligand coordinating the metal ion to its maximum extent. The Zn(II) center is coordinated in a distorted octahedral geometry by five atoms from H_2qp3 and an oxygen atom from a water molecule. The bond angles around the Zn(II) center do not deviate from the ideal octahedral values as much as they do for **2**. The pyridine rings from the ligand are *cis* to each other, whereas the bound H_2O is *trans* to one of the amines. As with **2**, the components within the asymmetric unit hydrogen bond extensively with each other, resulting in another dense crystal (1.626 g/cm^3). The non-coordinated OH group in the quinol donates a hydrogen bond to a triflate, while the metal-bound OH hydrogen bonds to an outer-sphere molecule of H_2O. The Zn(II)-bound H_2O hydrogen bonds to the second triflate, which is disordered over two positions. The quinol appears to aromatically interact with one of the pyridine rings; the centroids of the quinol and the pyridine ring containing N(2) are 3.59 Å apart.

Aqueous Solution Characterization. Neither of the solid-state structures of the Zn(II) complexes with H_2qp1 was found to be maintained in water, and the predominant aqueous species for **1** above pH 7 is $[Zn(Hqp1)]^+$, which features a metal-coordinated quinolate.[26] Because **2** and **3** are intended to be used as catalysts for the decomposition of superoxide in aqueous solutions, understanding their behavior in water is essential. We therefore determined the speciation of **2** and **3** in water using potentiometric and spectrophotometric pH titrations (Figures S9−S11).

The acid/base chemistry of the H_4qp2 ligand in water was previously described during our characterization of its complex with Mn(II).[22] The Zn(II) complex displays two clear ionization events as the pH increases from 2.5 to 10. These are consistent with pK_a values of 5.3 and 8.5, which we assign to the deprotonation of the two Zn(II)-bound quinols. The major species between pH 7.0 and 7.4 would therefore be $[Zn(H_3qp2)]^+$, where H_3qp2^- is the singly deprotonated form of the ligand. Unfortunately, we could not use these data to obtain stability constants for $[Zn(H_3qp2)]^+$ and $[Zn(H_2qp2)]$. The log(β) values for these species do not converge to stable numbers even after extensive attempts to fit the data to a wide variety of models using the speciation program Hyperquad. We had encountered similar difficulties modeling the data for $[Zn(H_2qp1)(OTf)]^+$.[26] The ability to calculate these values requires a substantial amount of the metal to dissociate from the ligand under acidic conditions; this does not appear to happen for either the H_2qp1 or H_4qp2 systems. Complex **2** is therefore more stable in water than its Mn(II) analogue, which does dissociate under similar treatment.[22]

The H_2qp3 ligand undergoes four ionization events as the pH is increased from 2.5 to 10 (Table 2 and Figure 2A). We have assigned these to four sequential deprotonations of H_5qp3^{3+}. The first three ionization events are associated with pK_a values of 3.5, 5.13, and 8.19 and likely correspond to the removal of protons from pyridinium and ammonium groups. The 10.2 pK_a value associated with the last ionization event is consistent with the deprotonation of a phenolic OH group, which would convert H_2qp3 into $Hqp3^-$. The error for this value is higher because the $Hqp3^-$ species did not fully form during the titration.

The Zn(II) complex with H_2qp3 appears to be stable above pH 5 (Figure 2B), and the pZn calculated for 1.0 mM ligand and 1.0 mM Zn(II) at pH 7.4 is 7.54. Below pH 5, the Zn(II) complex displays two ionization events. The first is assigned to the association/dissociation of Zn(II). We believe that the second ionization event observed with the increase in pH corresponds to the deprotonation of $[Zn(H_3qp3)]^{3+}$ to $[Zn(H_2qp3)]^{2+}$. The protonation of the ligand at low pH likely facilitates the loss of the metal ion under acidic conditions. The complex is further deprotonated as the pH rises past 5. The 5.57 pK_a value associated with the third ionization event is consistent with the deprotonation of a Zn(II)-bound quinol.[26] At pH 7 and above, the Zn(II) mostly exists as $[Zn(Hqp3)]^+$.

Electrochemistry. The redox behavior of **2** and **3** in aqueous phosphate solutions buffered to pH 7.0 was analyzed by CV. The CV for each complex displays a single feature. For complex **2**, the redox event has $E_{1/2}$ = 195 mV versus Ag/AgCl, with ΔE = 208 mV at a 100 mV/s scan rate (Figure S11).

https://doi.org/10.1021/acs.inorgchem.2c03256
Inorg. Chem. 2022, 61, 19983−19997

Table 2. Stability Constants and pK_a Values for the H_4qp2 and H_2qp3 Ligands and Their Zn(II) Complexes as Determined by Potentiometric Titration at 25 °C

H_4qp2		**Zn−H_4qp2**	
pK_{L1}[a]	7.18 (±0.03)	pK_{a1}[b]	5.3 (±0.3)
pK_{L2}[a]	4.47 (±0.08)	pK_{a2}[b]	8.5 (±0.3)
H_2qp3		**Zn−H_2qp3**	
pK_{L1}[a]	10.2 (±0.3)	pK_{a1}[b]	5.57 (±0.10)
pK_{L2}[a]	8.19 (±0.05)	pK_{a2}[b]	2.98 (±0.15)
pK_{L3}[a]	5.13 (±0.05)	log K(ZnHqp3)[c]	15.75
pK_{L4}[a]	3.5 (±0.3)	log K(ZnH_2qp3)[c]	11.14
		log K(ZnH_3qp3)	5.93

[a]Ligand pK_a values correspond to the following equilibrium constants:

H_4qp2
$K_{L1} = [(H_4qp2)][H^+]/[(H_5qp2)^+]$, from reference.
$K_{L2} = [(H_5qp2)^+][H^+]/[(H_6qp2)^{2+}]$, from reference.

H_2qp3
$K_{L1} = [(Hqp3)^-][H^+]/[(H_2qp3)]$, $pK_{L1} = \log\beta_{010} - \log\beta_{-110}$.
$K_{L2} = [(H_2qp3)][H^+]/[(H_3qp3)^+]$, $pK_{L2} = \log\beta_{110} - \log\beta_{010}$.
$K_{L3} = [(H_3qp3)^+][H^+]/[(H_4qp3)^{2+}]$, $pK_{L3} = \log\beta_{210} - \log\beta_{110}$.
$K_{L4} = [(H_4qp3)]^{2+}[H^+]/[(H_5qp3)^{3+}]$, $pK_{L4} = \log\beta_{310} - \log\beta_{210}$.

[b]Metal complex pK_a values correspond to the following equilibrium constants:

Zn-H_4qp2
$K_{a1} = [[Zn(H_3qp2)]^+][H^+]/[[Zn(H_4qp2)]^{2+}]$.
$K_{a2} = [[Zn(H_2qp2)]][H^+]/[[Zn(H_3qp2)]^+]$.

Zn-H_2qp3
$K_{a1} = [[Zn(Hqp3)]^+][H^+]/[[Zn(H_2qp3)]^{2+}]$, $pK_{a1} = \log\beta_{011} - \log\beta_{-111}$.
$K_{a2} = [[Zn(H_2qp3)]^{2+}][H^+]/[[Zn(H_3qp3)^{3+}]]$, $pK_{a12} = \log\beta_{111} - \log\beta_{011}$.

[c]Metal complex stability constants correspond to the following equilibrium constants:

$K(ZnHqp3) = [[Zn(Hqp3)]^+]/[Zn^{2+}][Hqp3^-]$
$K(ZnH_2qp3) = [[Zn(H_2qp3)]^{2+}]/[Zn^{2+}][H_2qp3]$
$K(ZnH_3qp3) = [[Zn(H_3qp3)^{3+}]]/[Zn^{2+}][H_3qp3^+]$

Complex **3** gives rise to a more reversible redox feature with $E_{1/2}$ = 150 mV versus Ag/AgCl and ΔE = 166 mV at a 100 mV/s scan rate (Figure S12). The peak-to-peak separations for both compounds become larger with faster scan rates, consistent with irreversible redox processes. The peak-to-peak separations increase more markedly for **2**, consistent with the redox for this complex being less reversible. Because the metal center is essentially redox-inactive, these features correspond to the oxidation of the quinols in the ligand to *para*-quinones and their subsequent reduction back to their original state.

Antioxidant Activity. Both **2** and **3** were initially screened using the xanthine oxidase/hypoxathine/lucigenin assay[22,23,38,44] and display above-baseline activity (Figure 3). The IC_{50} values for the elimination of the lucigenin sensing reaction were found to be within error of each other: 24 (±1) nM for **2** and 27 (±17) nM for **3**. The assay likewise does not meaningfully distinguish the antioxidant activities of **2** and **3** from those of the related complexes [Mn(H_4qp2)Br_2] (IC_{50} = 18 nM)[22] and **1** (IC_{50} = 17 nM).[26]

Complexes **2** and **3** were also analyzed with the DPPH assay (Figure 4), which tests the abilities of compounds to donate hydrogen atoms to 2,2-diphenyl-1-picrylhydrazyl radical hydrate.[39−41,45] In this assay, the production of the hydrazine is confirmed and followed by UV/vis. The IC_{50} values for **2** and **3** were measured to be 8.7 and 17.2 μM, respectively, with the H_4qp2 complex being substantially better as an antioxidant. The ascorbic acid standard had an IC_{50} value of 24.2 μM under the same conditions. Other divalent metal complexes with the H_2qp1 and H_4qp2 ligands likewise outperformed ascorbic acid in these measurements by approximately the same extent.[22,23,26]

The aforementioned assays, unfortunately, often provide misleading accounts of the actual reactivity with superoxide due to competing side-reactions between the various components in the reaction mixtures.[12,27,46−49] Consequently, the SOD mimicry was more thoroughly assessed by analyzing the direct reactions between the compounds and KO_2 (Figure 5 and Table 3). Complex **2** reacts directly with $O_2^{\cdot-}$ and accelerates its decomposition, but compound **3** is not a competent catalyst for superoxide disproportionation (Figure S13). The catalytic rate constants for **1** and **2** in various aqueous solutions are provided on Table 3. The activity improves when the solution is made more basic or the buffer is changed from a sulfonate derivative (HEPES, MOPS) to phosphate.

Mechanistic Analysis. When mixtures of **3** and KO_2 are analyzed by mass spectrometry, we find m/z features consistent with Zn(II)-free oxidized ligand but not any that are consistent with Zn(II) complexes with either H_2qp3 or its *para*-quinone counterpart qp3 (Figure S16). The data suggest that the initial oxidation of **3** by KO_2 to $[Zn(qp3)]^{2+}$ weakens the binding affinity of the ligand enough to destabilize the qp3 complex. Our control experiments indicate that free H_2qp3 by itself cannot catalyze superoxide degradation; consequently, we believe that the dissociation of the Zn(II) from the oxidized H_2qp3 ligand (qp3) halts catalysis.

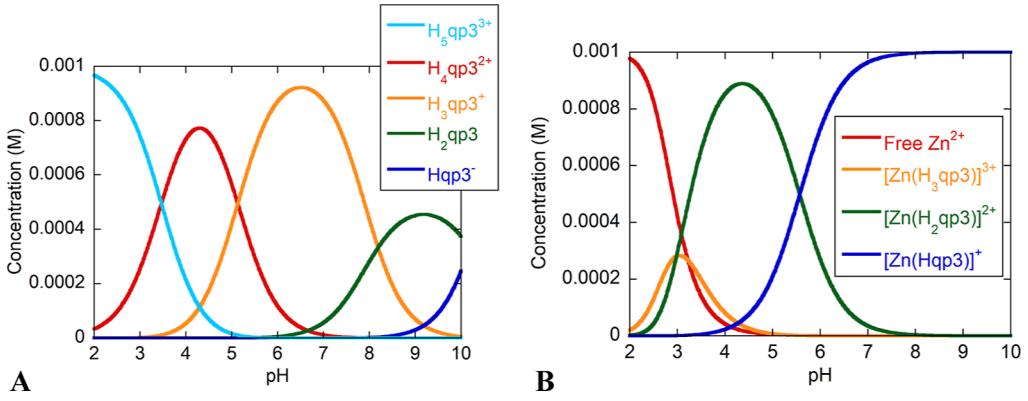

Figure 2. Predicted speciation as a function of pH for (A) 1.0 mM H_2qp3 and (B) a mixture of 1.0 mM H_2qp3 and 1.0 mM $ZnCl_2$ in 100 mM KCl solution.

https://doi.org/10.1021/acs.inorgchem.2c03256
Inorg. Chem. 2022, 61, 19983−19997

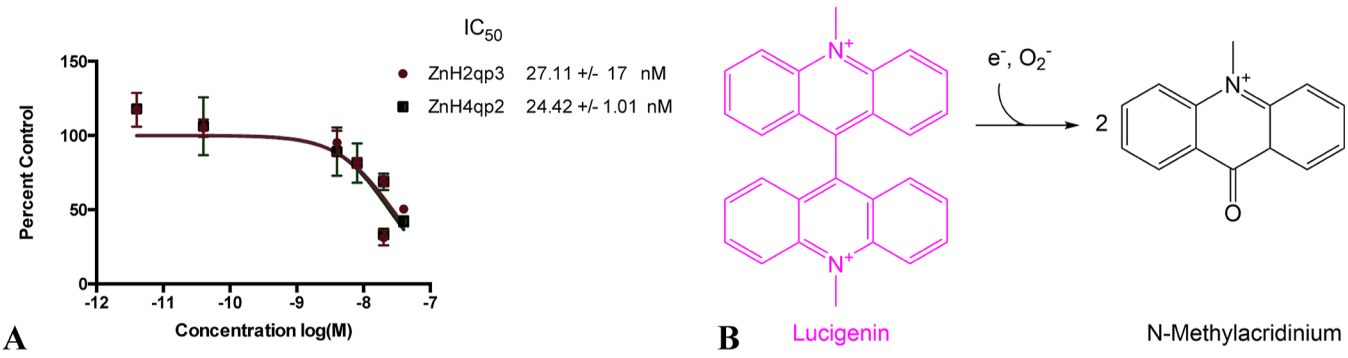

Figure 3. (A) Superoxide scavenging effects of **2** and **3**. Superoxide was generated using a hypoxanthine-xanthine oxidase reaction and detected using the chemiluminescent probe lucigenin. Reactions were carried out in 50 mM Tris−HCl (pH 8.0). Data for the various concentrations of Zn(II) complexes are expressed as a percentage of luminescence in the presence of vehicle. (B) Illustration of the fundamental reaction between lucigenin and superoxide. The depletion of lucigenin eliminates the observed chemiluminescence. The added SOD mimic competes with lucigenin for the superoxide.

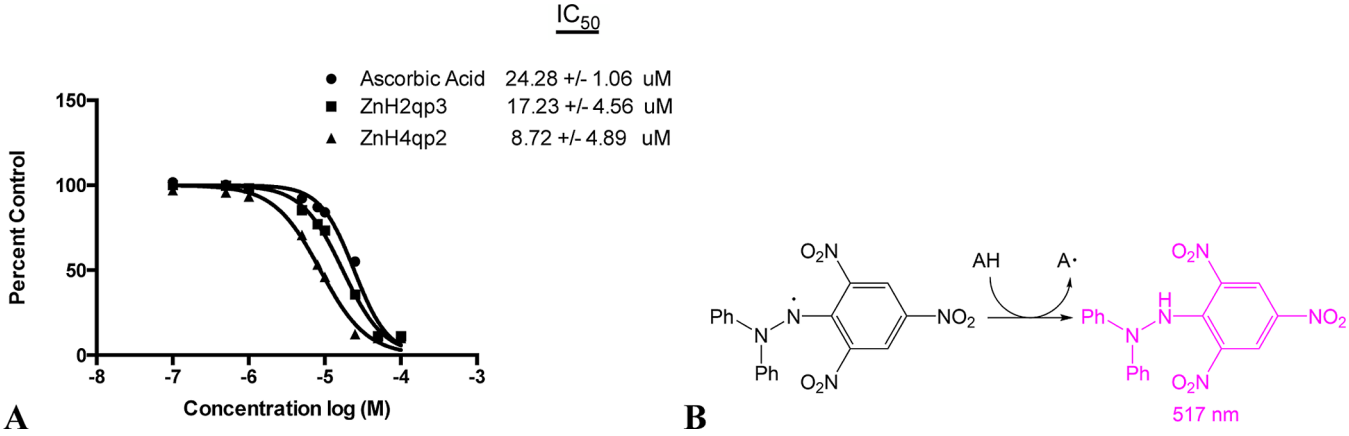

Figure 4. (A) DPPH free radical scavenging assay of **2**, **3**, and ascorbic acid. The antioxidants were added to DPPH and incubated in the dark for 30 min at 298 K. Spectroscopic measurements were performed at 517 nm. The data were normalized to the absorbance in the presence of vehicle. All experiments were performed in triplicate. (B) Illustration of the underlying chemical reaction between DPPH and an antioxidant (AH). H atom transfer from AH to the DPPH radical generates the visible hydrazine species.

We analyzed the reaction between the catalytically active **2** and KO_2 in MeCN by CSI-MS (Figure 6); all identified species are depicted on Scheme 3. $[Zn(H_4qp2)]^{2+}$ (HQ_1) and its conjugate base $[Zn(H_3qp2)]^{+}$ (HQ_2) are found under all conditions. When KO_2 is present, we observe m/z peaks consistent with oxidation to $[Zn(H_2qp2)]^{2+}$ (QH_1) and its subsequent deprotonation to $[Zn(Hqp2)]^{+}$ (QH_2). Although the ligand could conceivably be further oxidized to the di-*para*-quinone compound qp2, we do not detect any traces of either free qp2 or its complex with Zn(II) at either −40 °C or 0 °C. At 0 °C, we do find evidence for the oxidation of the benzylic or picolylic carbons on the ligand framework with both quinolate/quinol (HQ_{2ox}) and quinolate/*para*-quinone (QH_{2ox}) groups (Figure 7). We do not, however, observe any degradation products that would result from either N−C bond cleavage or dechelation (Figure 7).

Unexpectedly, we find traces of a Zn(II) complex with the mono-*para*-quinone form of the ligand (H_2qp2) in the absence of the superoxide. Aerobic solutions of metal-free H_4qp2 do not give rise to either the m/z peaks associated with H_2qp2.

When 0.10 mM **2** is mixed with excess KO_2 in MeCN at −40 °C and monitored by UV/vis, bands at 422 and 448 nm develop over 300 s (Figure 8). These features are characteristic of semiquinone (SQ) radicals.[50,51] Over longer periods of time (600 s), an additional band appears at 520 nm. The energy of this feature is reminiscent of the charge transfer complex quinhydrone (QH), which consists of a reduced hydroquinone interacting with an oxidized *para*-quinone.[52−54] Bands with almost exactly the same energies were observed for a Mn(II) complex with H_4qp2.[25] The intensities of all three features noticeably decrease by 1200 s.

We were able to independently generate a Zn(II)-ligand radical by reacting **2** with a base and a one-electron oxidant in MeCN. When 1.0 mM **2** reacts with 2.4 mM $Ag(SbF_6)$ and 235 mM Et_3N at 25 °C, we observe a strong signal at g = 2.0 (Figure S17) at 30 s; the g value is consistent with an organic radical. By 45 min, the feature decreases in intensity by approximately 50%. When we subjected **1** to similar treatment, we likewise observed a transient radical species, but the data differ from those for **2** in that the radical has almost completely vanished by 45 min. We also observed evidence of the generation of a semiquinone radical (SQ, Scheme 3) in the CSI-MS data shown in Figure 6B, where all three possible oxidation forms of the redox active ligand moiety, that is, hydroquinone, semiquinone, and *para*-quinone (quinhydrone), were detected in their protonated forms in the reaction mixture under catalytic conditions. Furthermore, the semiquinone species was detected by CSI-MS in the reaction between **2** and a 10-fold excess of H_2O_2. The reaction with H_2O_2 is orders of magnitude slower than the one with superoxide at 0 °C

https://doi.org/10.1021/acs.inorgchem.2c03256
Inorg. Chem. 2022, 61, 19983−19997

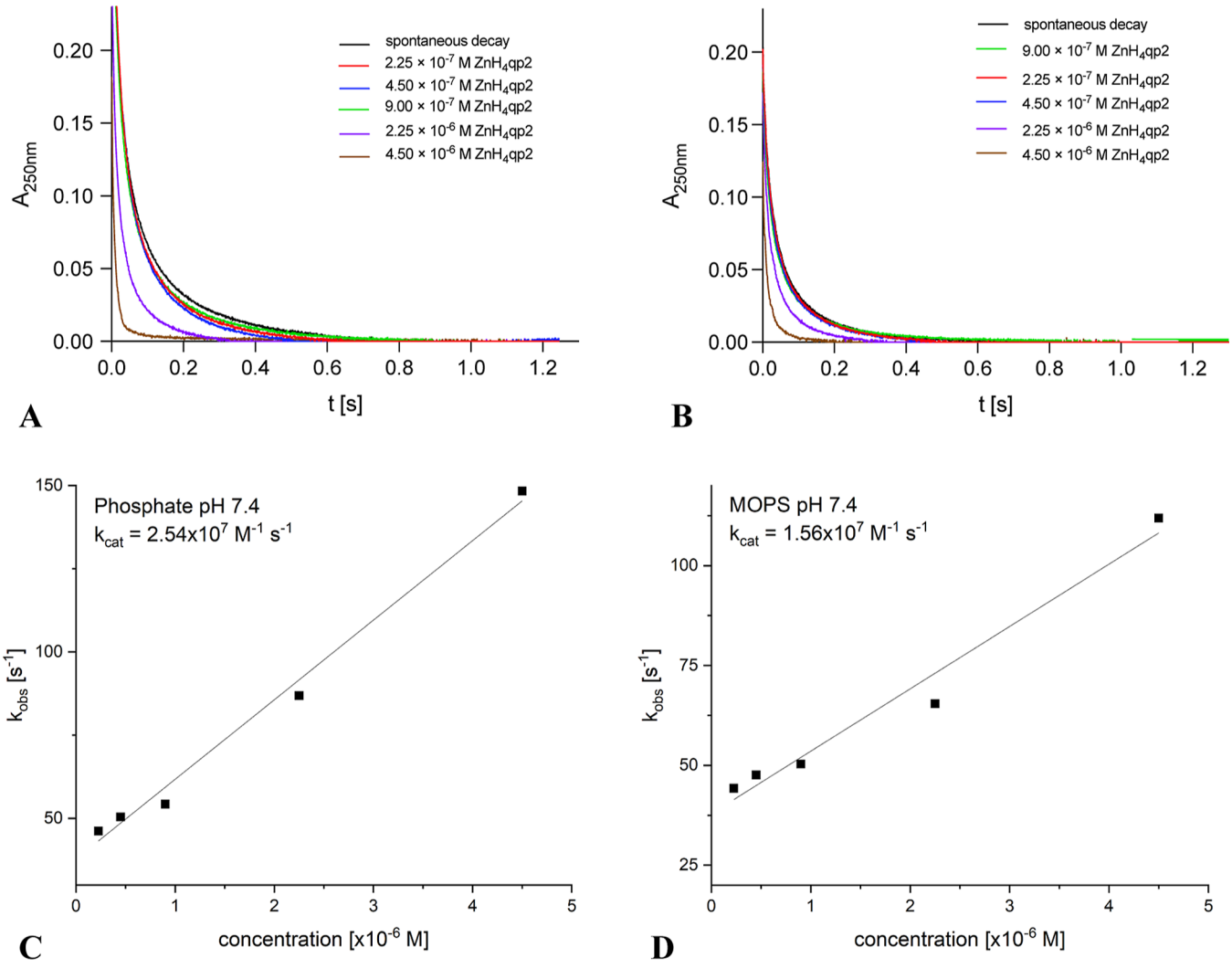

Figure 5. Kinetic traces of superoxide decomposition at 250 nm by **2**. (A) Data taken in 50 mM phosphate buffer, pH 7.4, ionic strength of 150 mM. The starting concentration of superoxide is 1.5×10^{-4} M. (B) Data taken in 60 mM MOPS buffer, pH 7.4, ionic strength of 150 mM. The starting concentration of superoxide is 9×10^{-5} M. (C) Plot of k_{obs} vs [**2**] for the pH 7.4 phosphate data. The k_{obs} values are calculated from the traces in panel A. (D) Plot of k_{obs} vs [**2**] for the pH 7.4 MOPS data. The k_{obs} values are calculated from the traces in panel B.

Table 3. Catalytic Rate Constants, k_{cat} (M^{-1} s^{-1}), Measured by Stopped-Flow Kinetics for the Direct Reactions of 1, 2, and 3 with Superoxide

buffer, pH	1[a]	2	3
60 mM HEPES/MOPS, 7.4	3.4×10^6	1.56×10^7	N.A.
60 mM MOPS, 7.8	N.D.	4.94×10^7	N.A.
60 mM HEPES, 8.1	4.7×10^6	N.D.	N.A.
50 mM phosphate, 7.4	1.9×10^7	2.54×10^7	N.A.

[a]Data from ref 26.

(Figure S18) and does not proceed with a measurable rate at −40 °C. Without the superoxide to serve as a reaction partner, the semiquinone intermediate undergoes self-decay, leading to almost complete degradation of the complex.

DISCUSSION

The recently characterized superoxide dismutase (SOD) mimic [Zn(H_2qp1)(OTf)](OTf) (**1**) is highly unusual in that it uses an organic component as the redox partner for the superoxide substrate and lacks a redox-active transition metal ion. Given the instability of most manganese-containing SOD mimics[31−33] and the potential toxicity of this metal in biological systems,[55] the absence of redox-active transition metal ions may make **1** and similar complexes attractive candidates for the clinical treatment of oxidative stress. In order to determine what structural features are required for functional SOD mimicry for this fundamentally new class of catalysts, we prepared Zn(II) complexes with the quinol-containing H_4qp2 and H_2qp3 ligands (Scheme 2). These molecules differ from H_2qp1 in that they either feature a second quinol in place of a pyridine (H_4qp2) or lack one pyridine altogether, being pentadentate rather than hexadentate (H_2qp3).

The syntheses of [Zn(H_4qp2)]$(OTf)_2$ (**2**) and [Zn(H_2qp3)-(H_2O)]$(OTf)_2$ (**3**) are relatively straightforward, and we can readily isolate crystalline samples of both complexes (Figure 1). The crystal structures of **2** and **3** differ from those of **1** in that the quinols bind directly to the Zn(II) center.[26] The structural data for **2** suggest that both quinols cannot coordinate tightly to the Zn(II) at the same time, for the Zn−O(4) bond length is much longer than a typical Zn−O bond.[56] Based on this and the other distortions from octahedral geometry, we speculate that the Zn(II) metal

https://doi.org/10.1021/acs.inorgchem.2c03256
Inorg. Chem. 2022, 61, 19983−19997

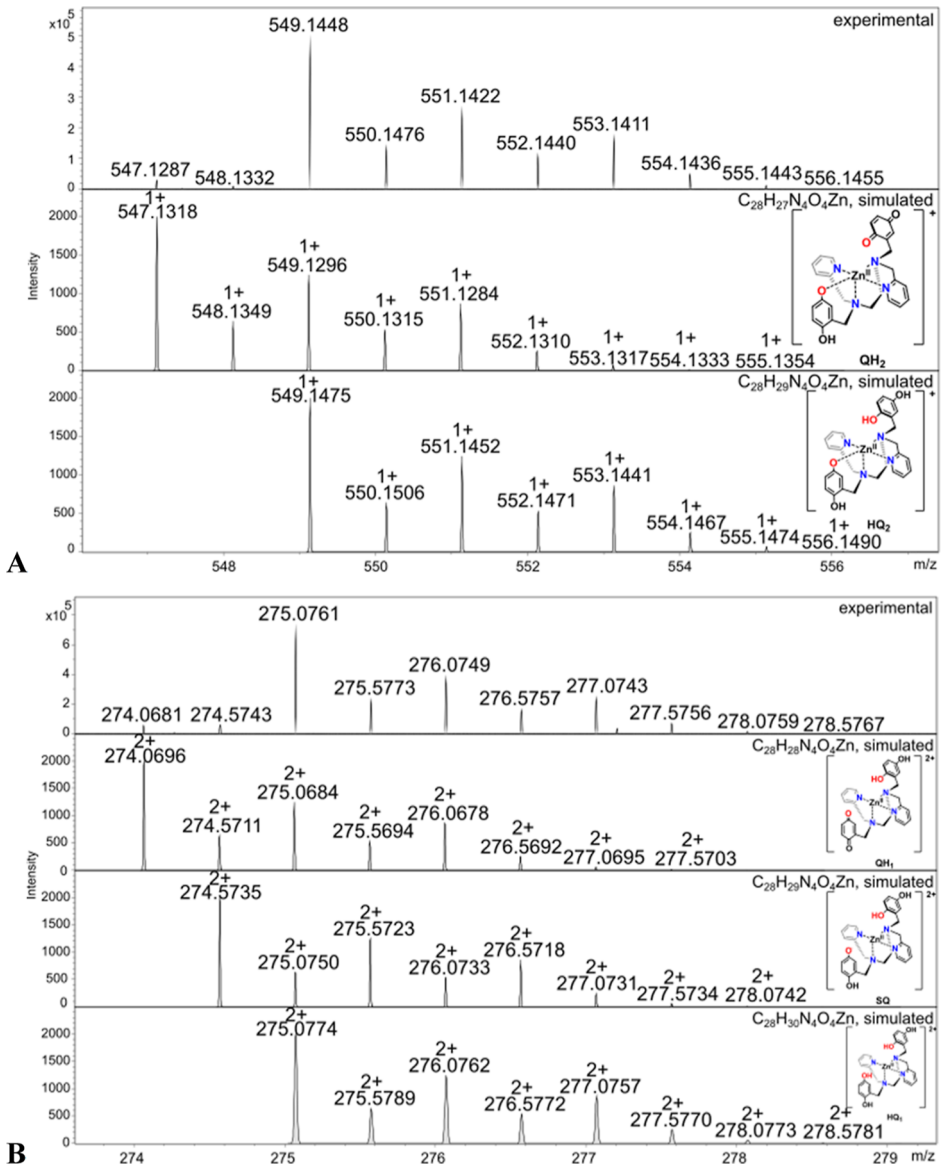

Figure 6. CSI-MS spectrometry of **2** upon reaction with KO_2. The graphics depict possible structures; we cannot preclude other modes of ligand coordination. The m/z = 556.1455 feature in **A** is assigned to $[Zn(H_3qp2)]^+$ (HQ_2, Scheme 3), the deprotonated form of the diquinol species $[Zn(H_4qp2)]^{2+}$ (HQ_1 in Scheme 3) which itself is assigned to the m/z = 275.0761 feature in **B**. The m/z = 547.1287 feature in **A** is assigned to $[Zn(Hqp2)]^+$ (QH_2, Scheme 3), the deprotonated form of the mono-*para*-quinone (existing as quinhydrone, *vide infra*) species $[Zn(H_2qp2)]^{2+}$ (QH_1, Scheme 3) which itself is assigned to the m/z = 274.0696 feature in **B**. The m/z = 274.5743 feature in **B** is assigned to a semiquinone radical species $[Zn(H_3qp2)]^{\cdot 2+}$ (SQ, Scheme 3). Experimental conditions: 1 mM solutions of **2** in MeCN (1% DMF) were cooled to −40 °C and then mixed with an excess of solid KO_2. After 6 min, the mixture was diluted in a pre-cooled syringe with pre-cooled MeCN to approximately 1×10^{-5} M and quickly injected into the mass spectrometer. The full range of data is shown in Figure S15.

center may be too small to be fully chelated by the H_4qp2 ligand. The NMR data for all three complexes are consistent with more than one conformer or coordination isomer existing in solution, suggesting that metal coordination by H_2qp1, H_4qp2, and H_2qp3 is both flexible and dynamic.

The weaker association of the second quinol with the Zn(II) appears to be maintained when **2** is dissolved in water. The first pK_a is consistent with a phenol ligated to a divalent metal (Table 2),[22,26,57] but the second measured pK_a value of 8.5 is much higher than anticipated and approaches the value of 10 expected for a non-metal-bound phenol. Both **2** and **3** appear to be stable in water, and the major species between pH 7.0 and 7.4 are Zn(II) complexes with singly deprotonated H_3qp2^- and $Hqp3^-$ ligands: $[Zn(H_3qp2)]^+$ and $[Zn(Hqp3)]^+$ (Figure 2).

Complex **2**, much like **1**, is particularly stable in water, with no metal dissociation observed even at low pH values.[26] The aqueous stabilities of both Zn(II) complexes compare highly favorably to those of the most active small molecule SOD mimics. The Mn(II) porphyrin complex $Mn^{II}Br_8TM\text{-}4\text{-}PyP^{4+}$, for instance, has been documented to be unstable at neutral pH, and the release of free manganese from the complex has hampered its path to clinical use.[31] Manganese complexes with pentaazamacrocycles represent the other major family of highly active SOD mimics. Arguably the best of these catalysts is M40401, which has a catalytic rate constant of approximately

https://doi.org/10.1021/acs.inorgchem.2c03256
Inorg. Chem. 2022, 61, 19983−19997

Scheme 3. Proposed Mechanism of Superoxide Dismutation Catalyzed by 2[a]

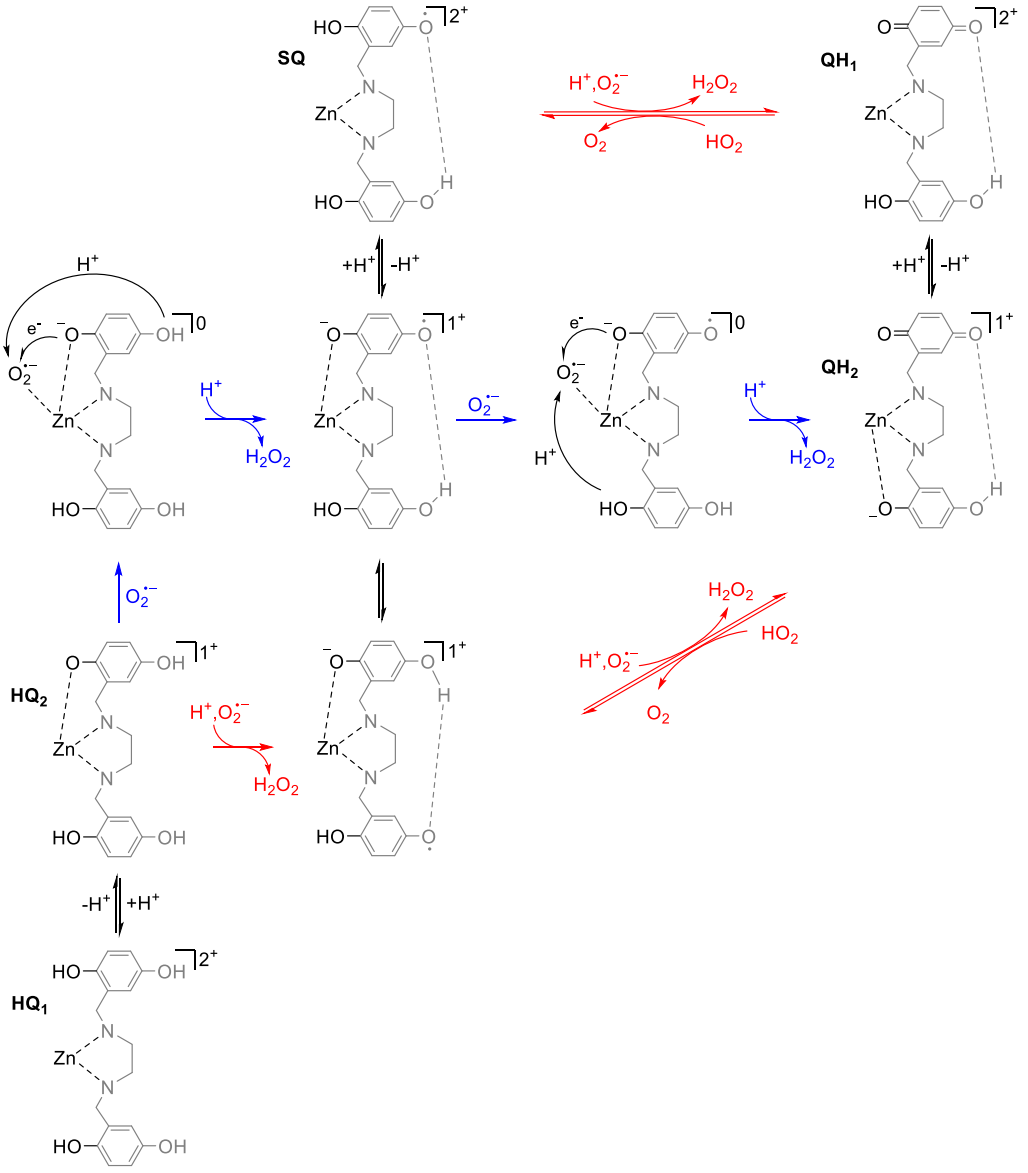

[a]Possible inner-sphere pathways are outlined in blue, whereas outer-sphere pathways are outlined in red. Hydroquinone and quinhydrone species HQ_1, HQ_2, QH_1, and QH_2, respectively, were detected under conditions of catalytic reaction with superoxide by CSI-MS, whereas a semiquinone species SQ was detected within an order of magnitude slower reaction with H_2O_2.

1.5×10^9 M^{-1} s^{-1}, but this compound likewise has limited conditional stability in water.[32,33]

Electrochemically, complexes **2** and **3** resemble **1** in that only a single reduction/oxidation couple is observed by CV (Figures S11 and S12).[26] The ligand structure, however, markedly impacts both $E_{1/2}$ and ΔE. The removal of a pyridine ring from the coordination environment increases $E_{1/2}$ from 312 mV versus NHE (**1**) to 347 mV versus NHE (**3**). This structural change also worsens the reversibility, with ΔE increasing from 95 mV (**1**) to 166 mV (**3**) with a 100 mV/s scan rate. The inclusion of another quinol in the coordination sphere raises $E_{1/2}$ further to 397 mV versus NHE (**2**), and this redox feature is the least reversible of the three observed for the Zn(II)-quinol complexes, with a ΔE of 208 mV with a 100 mV/s scan rate. The H_4qp2 ligand likewise gave rise to a much less reversible redox event than H_2qp1 when ligated to Mn(II), and the CV features observed for $[Mn(H_4qp2)Br_2]$ in water would be considered irreversible by most.[22,23] The ligand-derived redox couple seen for $[Mn(H_4qp2)Br_2]$, however, has an $E_{1/2}$ that is less positive than that of $[Mn(H_2qp1)(MeCN)]^{2+}$. Unlike **2**, both of the H_4qp2 quinols appear to tightly coordinate to the larger Mn(II) center in solution, providing an explanation for why the same decrease in $E_{1/2}$ is not observed for the Zn(II) complexes when the H_2qp1 ligand is replaced by H_4qp2.[22] In both **2** and **3**, the $E_{1/2}$ shifts away from the ∼300 mV ideal for SOD activity; these shifts and the lesser reversibility could potentially worsen the catalysis of $O_2^{\bullet-}$ degradation by an outer-sphere mechanism. That **2** is more catalytically active than **1**, despite the less reversible redox feature, suggests that the superoxide dismutation instead proceeds through a more efficient inner-sphere path.

Both **2** and **3** initially appeared to be competent SOD mimics when analyzed via the xanthine oxidase/hypoxanthine/lucigenin[38] and DPPH assays.[39−41,45] The IC_{50} values from

https://doi.org/10.1021/acs.inorgchem.2c03256
Inorg. Chem. 2022, 61, 19983−19997

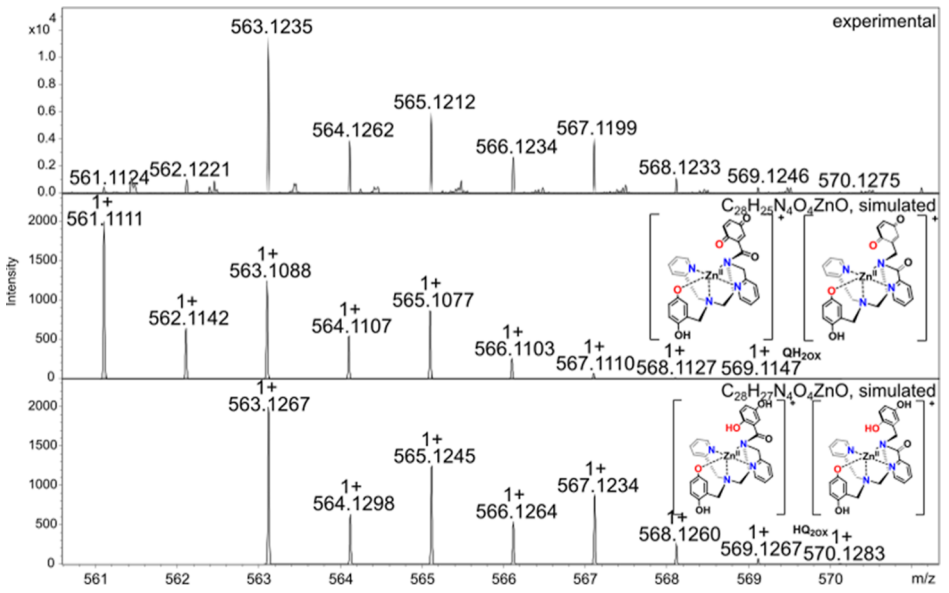

Figure 7. CSI-MS spectrometry of **2** upon a 6 min reaction with KO_2. The graphics depict possible structures; we cannot preclude other modes of ligand coordination. The m/z = 561.1124 feature is assigned to a Zn(II) complex with an oxidized *para*-quinone ligand (QH_{2ox}). Other m/z features are more consistent with Zn(II) complexes with oxidized forms of the quinol ligand (HQ_{2ox}). Experimental conditions: 1 mM solutions of **2** in MeCN (1% DMF) were cooled to −40 °C and then mixed with an excess of solid KO_2. After 6 min, the mixture was diluted in a pre-cooled syringe with pre-cooled MeCN to approximately 1×10^{-5} M and quickly injected into the mass spectrometer. The full range of data is shown in Figure S15.

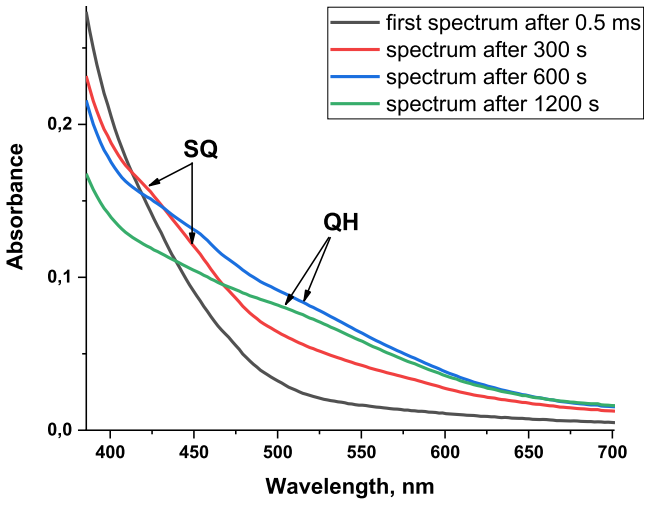

Figure 8. UV/vis data for the reaction between 0.10 mM **2** and excess KO_2 in MeCN at −40 °C.

these measurements (Figures 2 and 3) suggested that their abilities to behave as antioxidants were either comparable or only slightly inferior to those of the related compounds [Mn(H_4qp2)Br_2] and **1**.[22,26] The assay results, however, are misleading. When the direct reactions between the Zn(II) complexes and KO_2 are studied by stopped-flow kinetics methods, the data reveal that **2** is a markedly better catalyst than **1**, whereas **3** is not active enough to measurably increase the rate of $O_2^{\cdot-}$ disproportionation above that of the uncatalyzed reaction (Table 3).

Complex **2** is approximately fivefold more active in MOPS buffer than **1** in the comparable HEPES buffer. As with **1**, the catalysis of **2** proceeds more quickly in phosphate solution. The activities of **1** and **2** are more similar in phosphate buffered to pH 7.4, with **2** being 20% more active than **1**. Complexes **1** and **2** are unique among SOD mimics in that their activities are enhanced, rather than diminished in phosphate buffers.[24,27,28] Given the high prevalence of phosphate in mammalian cells, this represents a substantial advantage.[34,35] That the activity of **2** improves in phosphate buffer suggests that this is a replicable and trademark feature of Zn(II)-quinol SOD mimics that is not just limited to compound **1**. The improved activity in phosphate likely results from the substantially different speciations of the buffer components between pH 7 and 8. MOPS exists as a mixture of a neutral and a monoanionic species, whereas phosphate is a mixture of a monoanionic and a dianionic species. The greater overall negative charge on the phosphate-derived species facilitates their ability to interact with and transfer protons to and from the positively charged Zn(II) species on the mechanistic proton-coupled electron transfer cycle.

Curiously, replacing H_2qp1 with H_4qp2 worsens the SOD mimicry of manganese-containing complexes. Mn(II) is larger than Zn(II),[56] allowing H_4qp2 to fully coordinate the metal center. This in turn allows both quinols to approach the Mn(II) close enough to form strong Mn−O bonds, weakening the associated O−H bonds. With the manganese species, the ability of H_4qp2 to deprotonate to a dianionic form (H_2qp2^{2-}) renders its complexes with Mn(II) and Mn(III) less positive than the analogous complexes with Hqp1^-. The lesser overall positive charge hinders the ability of the Mn−H_4qp2 compounds to attract and bind $O_2^{\cdot-}$, thereby decreasing the rate of $O_2^{\cdot-}$ decomposition. The Zn(II)−H_4qp2 system differs from the Mn−H_4qp2 one in that the second quinol cannot approach the metal center as closely (Figure 1) which weakens the influence of the metal center on the acid/base properties of the quinol. The Zn(II)-for-Mn(II) substitution thereby raises the pK_a of the second quinol in the coordination complexes from 7.14 [Mn(II)][22] to 8.5 [Zn(II), Table 2]. The major species for **2** in water at pH 7.4 is consequently cationic [Zn(H_3qp2)]$^+$ rather than [Zn(H_2qp2)]. The Zn(II)-for-

https://doi.org/10.1021/acs.inorgchem.2c03256
Inorg. Chem. 2022, 61, 19983−19997

Mn(II) substitution also doubles the catalytic activity in pH 7.4 phosphate buffer.

The charge of the major species for **1** in pH 7.4 water, $[Zn(Hqp1)]^+$, is likewise +1, yet **1** is a less active catalyst, particularly in solutions using sulfonic acid-based buffers.[26] We speculate that the weak interaction between the second H_4qp2 quinol and the Zn(II) makes that particular coordination site on the metal center more accessible to exogenous ligands, such as $O_2^{\cdot-}$. Although H_4qp2 is hexadentate, the inability of the second quinol to attach firmly to Zn(II) gives the ligand some pentadentate character. All of the donor atoms from H_2qp1, conversely, coordinate strongly to the metal center, and this ligand is more strongly hexadentate as a consequence. With the relatively small size of the Zn(II) ion, the H_2qp1 ligand more efficiently blocks the access of $O_2^{\cdot-}$ to the metal center than H_4qp2. The more ready accessibility of the Zn(II) center in **2** leads to faster $O_2^{\cdot-}$ degradation.

The greater accessibility of the metal center in **2** relative to that in **1** may also explain why O_2 reactivity, albeit slight, is observed for the H_4qp2 complex. Recently, it has been found that O_2 coordination to Zn(II) could activate this oxidant toward reactivity with HS^-, promoting the formation of $H_2S_2^{\cdot-}$ and $O_2^{\cdot-}$ radicals and thereby the persulfidation of proteins containing Zn(II) cofactors.[36] Subsequently, it was demonstrated that a dinuclear zinc complex with labile coordination sites can bind $O_2^{\cdot-}$ and activate it toward the oxidation of an appended phenolate ligand to the corresponding phenoxyl radical.[58] The Zn(II) is essential to the reaction; the free phenolic ligand and superoxide do not react in bulk solution. The Zn(II) in **2** may similarly mediate electron transfer between dioxygen and the coordinated quinolate. Our findings represent another rather unusual instance of Zn(II) modulating redox processes via an inner-sphere metal-coupled/mediated electron transfer mechanism. Given the heavy prevalence of zinc in biology, it seems likely that the roles that this metal ion plays in regulating physiological redox processes have yet to be fully elucidated.

The lack of activity for **3** is proposed to result from the dissociation of the ligand from the Zn(II) after its initial oxidation by $O_2^{\cdot-}$. The H_2qp3 ligand essentially becomes tetradentate upon two-electron oxidation of the quinolate to a *para*-quinone (qp3). The loss of the strongly coordinating quinolate allows the anions from the MOPS and phosphate buffers to strip the metal ion from the polydentate ligand; the resultant Zn(II) salts then precipitate from the solution. MS analysis of the reaction mixtures confirms that the reaction with KO_2 produces metal-free oxidized ligand as the major product (Figure S16). The results suggest that this quinol-containing ligand, similar to H_2qp1,[26] needs to remain tightly bound to the Zn(II) in order for catalysis to proceed. The observation of oxidized ligand demonstrates that **3** can initially react with $O_2^{\cdot-}$, but the stopped-flow kinetics data suggest that the catalyst does not survive enough turnovers to noticeably impact the rate of $O_2^{\cdot-}$ disproportionation.

Unlike **3**, complex **2** maintains its catalysis after the initial round of oxidation. In addition to providing a readily accessible coordination site for $O_2^{\cdot-}$, the second quinol also serves as a replacement anionic ligand when the first quinol is oxidized to a *para*-quinone. The resultant complex, $[Zn(Hqp2)]^+$, where $Hqp2^-$ is a quinolate/*para*-quinone ligand (QH_2, Scheme 3), is stable enough to persist in water and continue to participate in catalysis, accounting for its higher activity. The second quinol in the ligand, similar to that in the related $[Mn(H_4qp2)Br_2]$, appears to resist oxidation.[25]

Although the higher activity of **2** relative to **1** may be consistent with an inner-sphere pathway, the MS and low-temperature UV/vis data cannot preclude outer-sphere reactions with $O_2^{\cdot-}$. Aside from Zn(II)−OOH species, the two pathways would yield the same intermediates (Scheme 3). Unlike **1**, we do not observe any m/z features that could correspond to Zn(II)−OOH species in reactions between **2** and KO_2.[26] The second quinol can potentially protonate putative Zn(II)−OOH species, and the concomitant coordination of the resultant quinolate may hasten H_2O_2 release enough to preclude detection of the short-lived hydroperoxo intermediate. The UV/vis data for these reactions are consistent with the formation of semiquinone (SQ) radical anions and quinhydrone (QH) species. The latter consists of the *para*-quinone interacting with the remaining quinol/quinolate. The semiquinone radical anions may also be stabilized through similar interactions.

Although **2** possesses two quinols, all of our data are consistent with only one of these serving as a redox partner for $O_2^{\cdot-}$ during catalysis. This said, the second quinol is essential to the observed activity for two reasons. First, its ability to deprotonate to an anionic quinolate helps to keep the oxidized ligand anchored to the Zn(II), preventing the initial oxidation of the ligand from halting catalysis as it does for **3**. Second, the UV/vis signatures suggest that the quinol/quinolate can hydrogen bond to and stabilize the radical species in the catalytic cycle.

CONCLUSIONS

The reactivity of the Zn(II)−H_4qp2 complex **2** demonstrates that the design strategy for SOD mimicry used for the Zn(II)−H_2qp1 complex **1**—using a redox-active ligand in place of a redox-active metal—is generally applicable and is not limited to a single catalyst. Low-temperature UV/vis provides evidence for the intermediacy of Zn(II)-semiquinone radicals, which were speculated but not directly observed in the catalysis performed by **1**. Although there are two redox-active organic groups in **2**, only one appears to participate as a redox partner for $O_2^{\cdot-}$ in the SOD mimicry. The replacement of one of the H_2qp1 pyridines with a quinol improves the activity in aqueous solutions buffered with sulfonic acids fivefold, likely by improving the accessibility of the metal center to $O_2^{\cdot-}$, facilitating the efficient release of H_2O_2 through a proton delivery associated with coordination of resulted quinolate, and assuring stability of the complex upon oxidation of the first quinol. Complex **2**, similar to **1**, functions better in phosphate buffer, differentiating these catalysts from manganese-containing SOD mimics and potentially making them more suitable for treating oxidative stress in vivo. Complex **3**, conversely, is not a successful SOD mimic due to the lesser stability of its oxidized form $[Zn(qp3)]^{2+}$. The inability of **3** to noticeably impact the rate of superoxide disproportionation demonstrates that merely having a mixture of a Zn(II) salt and a quinol/*para*-quinone compound is not sufficient for catalysis; the redox-active organic component needs to be closely associated with, if not covalently tethered to, the metal center for these reactions to succeed.

https://doi.org/10.1021/acs.inorgchem.2c03256
Inorg. Chem. 2022, 61, 19983−19997

■ ASSOCIATED CONTENT

Supporting Information

The Supporting Information is available free of charge at https://pubs.acs.org/doi/10.1021/acs.inorgchem.2c03256.

NMR spectra, MS spectra, IR spectra, pH titration data, and CV data for **2** and **3** (PDF)

Accession Codes

CCDC 1899770 and 1909028 contain the supplementary crystallographic data for this paper. These data can be obtained free of charge via www.ccdc.cam.ac.uk/data_request/cif, or by emailing data_request@ccdc.cam.ac.uk, or by contacting The Cambridge Crystallographic Data Centre, 12 Union Road, Cambridge CB2 1EZ, UK; fax: +44 1223 336033.

■ AUTHOR INFORMATION

Corresponding Authors

Ivana Ivanović-Burmazović − *Department Chemie, Ludwig-Maximilians Universität (LMU) München, München 81377, Germany*; Email: ivivch@cup.lmu.de

Christian R. Goldsmith − *Department of Chemistry and Biochemistry, Auburn University, Auburn, Alabama 36849, United States*; orcid.org/0000-0001-7293-1267; Email: crgoldsmith@auburn.edu

Authors

Jamonica L. Moore − *Department of Chemistry and Biochemistry, Auburn University, Auburn, Alabama 36849, United States*

Julian Oppelt − *Department Chemie, Ludwig- Maximilians Universität (LMU) München, München 81377, Germany*

Laura Senft − *Department Chemie, Ludwig- Maximilians Universität (LMU) München, München 81377, Germany*

Alicja Franke − *Department Chemie, Ludwig- Maximilians Universität (LMU) München, München 81377, Germany*

Andreas Scheitler − *Department of Chemistry and Pharmacy, University of Erlangen-Nürnberg, Erlangen 91508, Germany*

Meghan W. Dukes − *Department of Chemistry and Biochemistry, Auburn University, Auburn, Alabama 36849, United States*

Haley B. Alix − *Department of Chemistry and Biochemistry, Auburn University, Auburn, Alabama 36849, United States*

Alexander C. Saunders − *Department of Chemistry and Biochemistry, Auburn University, Auburn, Alabama 36849, United States*

Sana Karbalaei − *Department of Chemistry and Biochemistry, Auburn University, Auburn, Alabama 36849, United States*

Dean D. Schwartz − *Department of Anatomy, Physiology, and Pharmacology, College of Veterinary Medicine, Auburn University, Auburn, Alabama 36849, United States*

Complete contact information is available at: https://pubs.acs.org/10.1021/acs.inorgchem.2c03256

Author Contributions

⊥J.L.M. and J.O. contributed equally to this work.

Notes

The authors declare no competing financial interest.

■ ACKNOWLEDGMENTS

We thank Auburn University and the National Science Foundation (NSF-CHE-1662875 and NSF-CHE-1954336) for financially supporting this work. We also thank Ludwig-Maximilians University and the Bayerisches Staatsministerium für Wissenschaft und Kunst.

■ REFERENCES

(1) Ahmed, M. I.; Gladden, J. D.; Litovsky, S. H.; Lloyd, S. G.; Gupta, H.; Inusah, S.; Denney, T., Jr.; Powell, P.; McGiffin, D. C.; Dell'Italia, L. J. Increased Oxidative Stress and Cardiomyocyte Myofibrillar Degeneration in Patients with Chronic Isolated Mitral Regurgitation and Ejection Fraction >60. *J. Am. Coll. Cardiol.* **2010**, *55*, 671−679.

(2) Fearon, I. M.; Faux, S. P. Oxidative Stress and Cardiovascular Disease: Novel Tools Give (Free) Radical Insight. *J. Mol. Cell. Cardiol.* **2009**, *47*, 372−381.

(3) Eskici, G.; Axelsen, P. H. Copper and Oxidative Stress in the Pathogenesis of Alzheimer's Disease. *Biochemistry* **2012**, *51*, 6289−6311.

(4) Kinnula, V. L. Production and Degradation of Oxygen Metabolites During Inflammatory States in the Human Lung. *Curr. Drug Targets - Inflamm. Allergy* **2005**, *4*, 465−470.

(5) AbdulSalam, S. F.; Thowfeik, F. S.; Merino, E. J. Excessive Reactive Oxygen Species and Exotic DNA Lesions as an Exploitable Liability. *Biochemistry* **2016**, *55*, 5341−5352.

(6) Mosley, R. L.; Benner, E. J.; Kadiu, I.; Thomas, M.; Boska, M. D.; Hasan, K.; Laurie, C.; Gendelman, H. E. Neuroinflammation, Oxidative Stress, and the Pathogenesis of Parkinson's Disease. *Clin. Neurosci. Res.* **2006**, *6*, 261−281.

(7) Laforge, M.; Elbim, C.; Frère, C.; Hémadi, M.; Massaad, C.; Nuss, P.; Benoliel, J.-J.; Becker, C. Tissue Damage from Neutrophil-Induced Oxidative Stress in COVID-19. *Nat. Rev. Immunol.* **2020**, *20*, 515−516.

(8) Abouhashem, A. S.; Singh, K.; Azzazy, H. M. E.; Sen, C. K. Is Low Alveolar Type II Cell SOD3 in the Lungs of Elderly Linked to the Observed Severity of COVID-19? *Antioxid. Redox Signaling* **2020**, *33*, 59−65.

(9) Riley, D. P.; Weiss, R. H. Manganese Macrocyclic Ligand Complexes as Mimics of Superoxide Dismutase. *J. Am. Chem. Soc.* **1994**, *116*, 387−388.

(10) Riley, D. P.; Schall, O. F. Structure−Activity Studies and the Design of Synthetic Superoxide Dismutase (SOD) Mimetics as Therapeutics. *Adv. Inorg. Chem.* **2006**, *59*, 233−263.

(11) Riley, D. P.; Lennon, P. J.; Neumann, W. L.; Weiss, R. H. Toward the Rational Design of Superoxide Dismutase Mimics: Mechanistic Studies for the Elucidation of Substituent Effects on the Catalytic Activity of Macrocyclic Manganese(II) Complexes. *J. Am. Chem. Soc.* **1997**, *119*, 6522−6528.

(12) Riley, D. P. Functional Mimics of Superoxide Dismutase Enzymes as Therapeutic Agents. *Chem. Rev.* **1999**, *99*, 2573−2588.

(13) Tovmasyan, A.; Carballal, S.; Ghazaryan, R.; Melikyan, L.; Weitner, T.; Maia, C. G. C.; Reboucas, J. S.; Radi, R.; Spasojevic, I.; Benov, L.; Batinic-Haberle, I. Rational Design of Superoxide Dismutase (SOD) Mimics: The Evaluation of the Therapeutic Potential of New Cationic Mn Porphyrins with Linear and Cyclic Substituents. *Inorg. Chem.* **2014**, *53*, 11467−11483.

(14) Batinic-Haberle, I.; Reboucas, J. S.; Spasojevic, I. Superoxide Dismutase Mimics: Chemistry, Pharmacology, and Therapeutic Potential. *Antioxid. Redox Signaling* **2010**, *13*, 877−918.

(15) Batinic-Haberle, I.; Rajic, Z.; Tovmasyan, A.; Reboucas, J. S.; Ye, X.; Leong, K. W.; Dewhirst, M. W.; Vujaskovic, Z.; Benov, L.; Spasojevic, I. Diverse Functions of Cationic Mn(III) N-substituted Pyridylporphyrins, Recognized as SOD Mimics. *Free Rad. Biol. Med.* **2011**, *51*, 1035−1053.

(16) Abreu, I. A.; Cabelli, D. E. Superoxide Dismutases- A Review of the Metal-Associated Mechanistic Variations. *Biochim. Biophys. Acta* **2010**, *1804*, 263−274.

(17) Policar, C.; Bouvet, J.; Bertrand, H. C.; Delsuc, N. SOD Mimics: From the Tool Box of the Chemists to Cellular Studies. *Curr. Opin. Chem. Biol.* **2022**, *67*, 102109.

(18) Robinett, N. G.; Peterson, R. L.; Culotta, V. C. Eukaryotic Copper-Only Superoxide Dismutases (SODs): A New Class of SOD

Enzymes and SOD-Like Protein Domains. *J. Biol. Chem.* **2018**, *293*, 4636−4643.
(19) Potter, S. Z.; Zhu, H.; Shaw, B. F.; Rodriguez, J. A.; Doucette, P. A.; Sohn, S. H.; Durazo, A.; Faull, K. F.; Gralla, E. B.; Nersissian, A. M.; Valentine, J. S. Binding of a Single Zinc Ion to One Subunit of Copper−Zinc Superoxide Dismutase Apoprotein Substantially Influences the Structure and Stability of the Entire Homodimeric Protein. *J. Am. Chem. Soc.* **2007**, *129*, 4575−4583.
(20) Ellerby, L. M.; Cabelli, D. E.; Graden, J. A.; Valentine, J. S. Copper−Zinc Superoxide Dismutase: Why Not pH-Dependent? *J. Am. Chem. Soc.* **1996**, *118*, 6556−6561.
(21) Yu, M.; Beyers, R. J.; Gorden, J. D.; Cross, J. N.; Goldsmith, C. R. A Magnetic Resonance Imaging Contrast Agent Capable of Detecting Hydrogen Peroxide. *Inorg. Chem.* **2012**, *51*, 9153−9155.
(22) Yu, M.; Ward, M. B.; Franke, A.; Ambrose, S. L.; Whaley, Z. L.; Bradford, T. M.; Gorden, J. D.; Beyers, R. J.; Cattley, R. C.; Ivanović-Burmazović, I.; Schwartz, D. D.; Goldsmith, C. R. Adding a Second Quinol to a Redox-Responsive MRI Contrast Agent Improves Its Relaxivity Response to H_2O_2. *Inorg. Chem.* **2017**, *56*, 2812−2826.
(23) Yu, M.; Ambrose, S. L.; Whaley, Z. L.; Fan, S.; Gorden, J. D.; Beyers, R. J.; Schwartz, D. D.; Goldsmith, C. R. A Mononuclear Manganese(II) Complex Demonstrates a Strategy to Simultaneously Image and Treat Oxidative Stress. *J. Am. Chem. Soc.* **2014**, *136*, 12836−12839.
(24) Kenkel, I.; Franke, A.; Dürr, M.; Zahl, A.; Dücker-Benfer, C.; Langer, J.; Filipović, M. R.; Yu, M.; Puchta, R.; Fiedler, S. R.; Shores, M. P.; Goldsmith, C. R.; Ivanović-Burmazović, I. Switching between Inner- and Outer-Sphere PCET Mechanisms of Small Molecule Activation: Superoxide Dismutation and Oxygen/Superoxide Reduction Reactivity Deriving from the Same Manganese Complex. *J. Am. Chem. Soc.* **2017**, *139*, 1472−1484.
(25) Senft, L.; Moore, J. L.; Franke, A.; Fisher, K. R.; Scheitler, A.; Zahl, A.; Puchta, R.; Fehn, D.; Ison, S.; Sader, S.; Ivanović-Burmazović, I.; Goldsmith, C. R. Quinol-Containing Ligands Enable High Superoxide Dismutase Activity by Modulating Coordination Number, Charge, Oxidation States and Stability of Manganese Complexes throughout Redox Cycling. *Chem. Sci.* **2021**, *12*, 10483−10500.
(26) Ward, M. B.; Scheitler, A.; Yu, M.; Senft, L.; Zillmann, A. S.; Gorden, J. D.; Schwartz, D. D.; Ivanović-Burmazović, I.; Goldsmith, C. R. Superoxide Dismutase Activity Enabled by a Redox-Active Ligand rather than a Metal. *Nat. Chem.* **2018**, *10*, 1207−1212.
(27) Friedel, F. C.; Lieb, D.; Ivanović-Burmazović, I. Comparative Studies on Manganese-Based SOD Mimetics, Including the Phosphate Effect, by Using Global Spectral Analysis. *J. Inorg. Biochem.* **2012**, *109*, 26−32.
(28) Lieb, D.; Friedel, F. C.; Yawer, M.; Zahl, A.; Khusniyarov, M. M.; Heinemann, F. W.; Ivanović-Burmazović, I. Dinuclear Seven-Coordinate Mn(II) Complexes: Effect of Manganese(II)-Hydroxo Species on Water Exchange and Superoxide Dismutase Activity. *Inorg. Chem.* **2013**, *52*, 222−236.
(29) Irving, H.; Williams, R. J. P. 637. The Stability of Transition-Metal Complexes. *J. Chem. Soc.* **1953**, 3192−3210.
(30) Martell, A. E.*Critical Stability Constants*; Plenum Press: New York, NY, 1974.
(31) Batinic-Haberle, I.; Spasojevic, I. 25 Years of Development of Mn Porphyrins — from Mimics of Superoxide Dismutase Enzymes to Thiol Signaling to Clinical Trials: The Story of Our Life in the USA. *J. Porphyr. Phthalocyanines* **2019**, *23*, 1326−1335.
(32) Salvemini, D.; Wang, Z.-Q.; Zweier, J. L.; Samouilov, A.; Macarthur, H.; Misko, T. P.; Currie, M. G.; Cuzzocrea, S.; Sikorski, J. A.; Riley, D. P. A Nonpeptidyl Mimic of Superoxide Dismutase with Therapeutic Activity in Rats. *Science* **1999**, *286*, 304−306.
(33) Aston, K.; Rath, N.; Naik, A.; Slomczynska, U.; Schall, O. F.; Riley, D. P. Computer-Aided Design (CAD) of Mn(II) Complexes: Superoxide Dismutase Mimetics with Catalytic Activity Exceeding the Native Enzyme. *Inorg. Chem.* **2001**, *40*, 1779−1789.
(34) Bergwitz, C.; Jüppner, H. Phosphate Sensing. *Adv. Chron. Kidney Dis.* **2011**, *18*, 132−144.
(35) Bevington, A.; Mundy, K. I.; Yates, A. J. P.; Kanis, J. A.; Russell, R. G. G.; Taylor, D. J.; Rajagopalan, B.; Radda, G. K. A Study of Intracellular Orthophosphate Concentration in Human Muscle and Erythrocytes by ^{31}P Nuclear Magnetic Resonance Spectroscopy and Selective Chemical Assay. *Clin. Sci.* **1986**, *71*, 729−735.
(36) Lange, M.; Ok, K.; Shimberg, G. D.; Bursac, B.; Markó, L.; Ivanović-Burmazović, I.; Michel, S. L. J.; Filipovic, M. R. Direct Zinc Finger Protein Persulfidation by H_2S Is Facilitated by Zn^{2+}. *Angew. Chem., Int. Ed.* **2019**, *58*, 7997−8001.
(37) Gans, P.; Sabatini, A.; Vacca, A. Investigation of equilibria in solution. Determination of equilibrium constants with the HYPERQUAD suite of programs. *Talanta* **1996**, *43*, 1739−1753.
(38) McCord, J. M.; Fridovich, I. Superoxide Dismutase: An Enzymic Function for Erythrocuprein (Hemocuprein). *J. Biol. Chem.* **1969**, *244*, 6049−6055.
(39) Kedare, S. B.; Singh, R. P. Genesis and Development of DPPH Method of Antioxidant Assay. *J. Food Sci. Technol.* **2011**, *48*, 412−422.
(40) Blois, M. S. Antioxidant Determinations by Use of a Stable Free Radical. *Nature* **1958**, *181*, 1199−1200.
(41) Milaeva, E. R.; Shpakovsky, D. B.; Gracheva, Y. A.; Orlova, S. I.; Maduar, V. V.; Tarasevich, B. N.; Meleshonkova, N. N.; Dubova, L. G.; Shevtsova, E. F. Metal Complexes with Functionalised 2,2′-Dipicolylamine Ligand Containing an Antioxidant 2,6-Di-*tert*-butylphenol Moiety: Synthesis and Biological Studies. *Dalton Trans.* **2013**, *42*, 6817−6828.
(42) Bielski, B. H. J.; Cabelli, D. E.; Arudi, R. L.; Ross, A. B. Reactivity of HO_2/O_2^- Radicals in Aqueous Solution. *J. Phys. Chem. Ref. Data* **1985**, *14*, 1041−1100.
(43) Chan, T.-L.; Mak, T. C. W. X-Ray Crystallographic Study of Guest-Molecule Orientations in the *β*-Hydroquinone Clathrates of Acetonitrile and Methyl Isocyanide. *J. Chem. Soc., Perkin Trans.* **1983**, *2*, 777−781.
(44) Iranzo, O. Manganese Complexes Displaying Superoxide Dismutase Activity: A Balance between Different Factors. *Bioorg. Chem.* **2011**, *39*, 73−87.
(45) Ancerewicz, J.; Migliavacca, E.; Carrupt, P.-A.; Testa, B.; Brée, F.; Zini, R.; Tillement, J.-P.; Labidalle, S.; Guyot, D.; Chauvet-Monges, A.-M.; Crevat, A.; Le Ridant, A. Structure-Property Relationships of Trimetazidine Derivatives and Model Compounds as Potential Antioxidants. *Free Rad. Biol. Med.* **1998**, *25*, 113−120.
(46) Fridovich, I. Superoxide Anion Radical (O_2^-), Superoxide Dismutases, and Related Matters. *J. Biol. Chem.* **1997**, *272*, 18515−18517.
(47) Liochev, S. I. Superoxide Dismutase Mimics, Other Mimics, Antioxidants, Prooxidants, and Related Matters. *Chem. Res. Toxicol.* **2013**, *26*, 1312−1319.
(48) Riley, D. P.; Rivers, W. J.; Weiss, R. H. Stopped-Flow Kinetic Analysis for Monitoring Superoxide Decay in Aqueous Systems. *Anal. Biochem.* **1991**, *196*, 344−349.
(49) Liochev, S. I.; Fridovich, I. Lucigenin (Bis-N-methylacridinium) as a Mediator of Superoxide Anion Production. *Arch. Biochem. Biophys.* **1997**, *337*, 115−120.
(50) Swallow, A. J.Physical Chemistry of Semiquinones. In *Functions of Quinones in Energy Converting Systems*; Trumpower, B. L., Ed.; Elsevier, Inc.: New York, NY, 1982, pp 59−72.
(51) Zhao, X.; Imahori, H.; Zhan, C.-G.; Sakata, Y.; Iwata, S.; Kitagawa, T. Resonance Raman and FTIR Spectra of Isotope-Labeled Reduced 1,4-Benzoquinone and Its Protonated Forms in Solutions. *J. Phys. Chem. A* **1997**, *101*, 622−631.
(52) Slifkin, M. A.*Charge Transfer Interactions of Biomolecules*; Academic Press: London, 1971.
(53) González Moa, M. J.; Mandado, M.; Mosquera, R. A. A Computational Study on the Stacking Interaction in Quinhydrone. *J. Phys. Chem. A* **2007**, *111*, 1998−2001.
(54) Regeimbal, J.; Gleiter, S.; Trumpower, B. L.; Yu, C.-A.; Diwakar, M.; Ballou, D. P.; Bardwell, J. C. A. Disulfide Bond Formation Involves a Quinhydrone-Type Charge−Transfer Complex. *Proc. Natl. Acad. Sci. U.S.A.* **2003**, *100*, 13779−13784.

https://doi.org/10.1021/acs.inorgchem.2c03256
Inorg. Chem. 2022, 61, 19983−19997

(55) Chen, P.; Chakraborty, S.; Mukhopadhyay, S.; Lee, E.; Paoliello, M. M. B.; Bowman, A. B.; Aschner, M. Manganese Homeostasis in the Nervous System. *J. Neurochem.* **2015**, *134*, 601−610.
(56) Shannon, R. D. Revised Effective Ionic Radii and Systematic Studies of Interatomic Distances in Halides and Chalcogenides. *Acta Crystallogr.* **1976**, *32*, 751−767.
(57) Gale, E. M.; Mukherjee, S.; Liu, C.; Loving, G. S.; Caravan, P. Structure-Redox-Relaxivity Relationships for Redox Responsive Manganese-Based Magnetic Resonance Imaging Probes. *Inorg. Chem.* **2014**, *53*, 10748−10761.
(58) Squarcina, A.; Fehn, D.; Senft, L.; Langer, J.; Ivanović-Burmazović, I. Dinuclear Zn Complex: Phenoxyl Radical Formation Driven by Superoxide Coordination. *Z. Anorg. Allg. Chem.* **2021**, *647*, 809−814.

https://doi.org/10.1021/acs.inorgchem.2c03256
Inorg. Chem. 2022, 61, 19983−19997